

Editing Conditional Radiance Fields

Steven Liu¹ Xiuming Zhang¹ Zhoutong Zhang¹ Richard Zhang² Jun-Yan Zhu^{2,3} Bryan Russell²
¹MIT ²Adobe Research ³CMU

Abstract

A neural radiance field (NeRF) is a scene model supporting high-quality view synthesis, optimized per scene. In this paper, we explore enabling user editing of a category-level NeRF – also known as a conditional radiance field – trained on a shape category. Specifically, we introduce a method for propagating coarse 2D user scribbles to the 3D space, to modify the color or shape of a local region. First, we propose a conditional radiance field that incorporates new modular network components, including a shape branch that is shared across object instances. Observing multiple instances of the same category, our model learns underlying part semantics without any supervision, thereby allowing the propagation of coarse 2D user scribbles to the entire 3D region (e.g., chair seat). Next, we propose a hybrid network update strategy that targets specific network components, which balances efficiency and accuracy. During user interaction, we formulate an optimization problem that both satisfies the user’s constraints and preserves the original object structure. We demonstrate our approach on various editing tasks over three shape datasets and show that it outperforms prior neural editing approaches. Finally, we edit the appearance and shape of a real photograph and show that the edit propagates to extrapolated novel views.

1. Introduction

3D content creation often involves manipulating high-quality 3D assets for visual effects or augmented reality applications, and part of a 3D artist’s workflow consists of making local adjustments to a 3D scene’s appearance and shape [26, 28]. Explicit representations give artists control of the different elements of a 3D scene. For example, the artist may use mesh processing tools to make local adjustments to the scene geometry or change the surface appearance by manipulating a texture atlas [62]. In an artist’s workflow, such explicit representations are often created by hand or procedurally generated.

While explicit representations are powerful, there remain significant technical challenges in automatically acquiring a high-quality explicit representation of a real-world

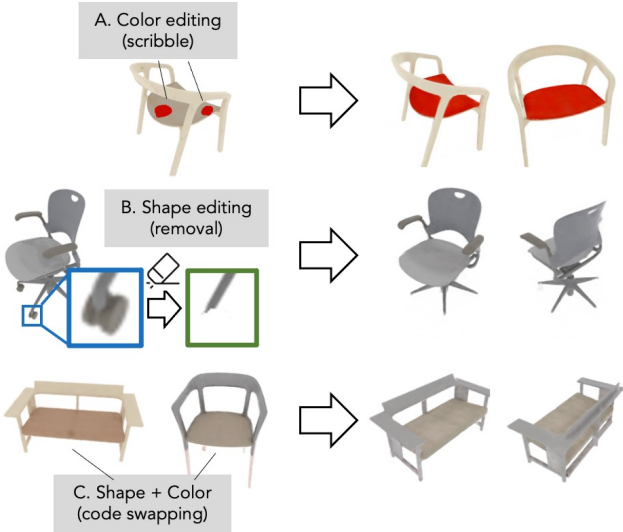


Figure 1: **Editing a conditional radiance field.** Given a conditional radiance field trained over a class of objects, we demonstrate three editing applications: (A) color editing, (B) shape editing, and (C) color/shape transfer. A user provides coarse scribbles over a local region of interest or selects a target object instance. Local edits propagate to the desired region in 3D and are consistent across different rendered views.

scene due to view-dependent appearance, complex scene topology, and varying surface opacity. Recently, implicit continuous volumetric representations have shown high-fidelity capture and rendering of a variety of 3D scenes and overcome many of the aforementioned technical challenges [50, 66, 45, 59, 63]. Such representations encode the captured scene in the weights of a neural network. The neural network learns to render view-dependent colors from point samples along cast rays, with the final rendering obtained via alpha compositing [58]. This representation enables many photorealistic view synthesis applications [41, 47]. However, we lack critical knowledge in how to enable artists’ control and editing in this representation.

Editing an implicit continuous volumetric representation is challenging. First, how can we effectively propagate sparse 2D user edits to fill the entire corresponding 3D region in this representation? Second, the neural network for an implicit representation has millions of parameters. It is unclear

which parameters control the different aspects of the rendered shape and how to change the parameters according to the sparse local user input. While prior work for 3D editing primarily focuses on editing an explicit representation [62], they do not apply to neural representations.

In this paper, we study how to enable users to edit and control an implicit continuous volumetric representation of a 3D object. As shown in Figure 1, we consider three types of user edits: (i) changing the appearance of a local part to a new target color (e.g., changing the chair seat’s color from beige to red), (ii) modifying the local shape (e.g., removing a chair’s wheel or swapping in new arms from a different chair), and (iii) transferring the color or shape from a target object instance. The user performs 2D local edits by scribbling over the desired location of where the edit should take place and selecting a target color or local shape.

We address the challenges in editing an implicit continuous representation by investigating how to effectively update a conditional radiance field to align with a target local user edit. We make the following contributions. First, we learn a conditional radiance field over an entire object class to model a rich prior of plausible-looking objects. Unexpectedly, this prior often allows the propagation of sparse user scribble edits to fill a selected region. We demonstrate complex edits without the need to impose explicit spatial or boundary constraints. Moreover, the edits appear consistently when the object is rendered from different viewpoints. Second, to more accurately reconstruct shape instances, we introduce a shape branch in the conditional radiance field that is shared across object instances, which implicitly biases the network to encode a shared representation whenever possible. Third, we investigate which parts of the conditional radiance field’s network affect different editing tasks. We show that shape and color edits can effectively take place in the later layers of the network. This finding motivates us to only update these layers and enables us to produce effective user edits with significant computational speed-up. Finally, we introduce color and shape editing losses to satisfy the user-specified targets, while preserving the original object structure.

We demonstrate results on three shape datasets with varying levels of appearance, shape, and training view complexity. We show the effectiveness of our approach for object view synthesis as well as color and shape editing, compared to prior neural editing methods. Moreover, we show that we can edit the appearance and shape of a real photograph and that the edit propagates to extrapolated novel views. We highly encourage viewing our [video](#) to see our editing demo in action. Code and more results are available at our [GitHub](#) repo and [website](#).

2. Related Work

Our work is related to novel view synthesis and interactive appearance and shape editing, which we review here.

Novel view synthesis. Photorealistic view synthesis has a storied history in computer graphics and computer vision, which we briefly summarize here. The goal is to infer the scene structure and view-dependent appearance given a set of input views. Prior work reasons over an explicit [11, 15, 22, 72] or discrete volumetric [20, 33, 36, 40, 44, 55, 64, 65, 67, 68, 80, 82] representation of the underlying geometry. However, both have fundamental limitations – explicit representations often require fixing the structure’s topology and have poor local optima, while discrete volumetric approaches scale poorly to higher resolutions.

Instead, several recent approaches implicitly encode a continuous volumetric representation of shape [14, 21, 38, 39, 42, 43, 48, 50, 54, 61] or both shape and view-dependent appearance [41, 45, 47, 59, 63, 66, 69, 76, 12, 73] in the weights of a neural network. These latter approaches overcome the aforementioned limitations and have resulted in impressive novel-view renderings of complex real-world scenes. Closest to our approach is Schwarz *et al.* [63, 12], where they build a generative radiance field over an object class and include latent vectors for the shape and appearance of an instance. Different from their methods, we include an instance-agnostic branch in our neural network, which inductively biases the network to capture common features across the shape class. As we will demonstrate, this inductive bias more accurately captures the shape and appearance of the class. Moreover, we do not require an adversarial loss to train our network and instead optimize a photometric loss, which allows our approach to directly align to a single view of a novel instance. Finally, our work is the first to address the question of how to enable a user to make local edits in this new representation.

Interactive appearance and shape editing. There has been much work on interactive tools for selecting and cloning regions [2, 35, 56, 60] and editing single still images [3, 6, 7, 34]. Recent works have focused on integrating user interactions into deep networks either through optimization [1, 9, 81, 10] or a feed-forward network with user-guided inputs [79, 57, 52, 49]. Here, we are concerned with editing 3D scenes, which has received much attention in the computer graphics community. Example interfaces include 3D shape drawing and shape editing using inflation heuristics [27], stroke alignment to a depicted shape [13], and learned volumetric prediction from multi-view user strokes [16]. There has also been work to edit the appearance of a 3D scene, e.g., via transferring multi-channel edits to other views [24], scribble-based material transfer [4], editing 3D shapes in a voxel representation [37], and relighting a scene with a paint brush interface [53]. Finally, there has been work on editing light fields [25, 29, 30]. We encourage the interested reader to review this survey on artistic editing of appearance, lighting, and material [62]. These prior works operate over light fields or explicit/discrete volumetric ge-

ometry whereas we seek to incorporate user edits in learned implicit continuous volumetric representations.

A closely related concept is edit propagation [3, 19, 23, 74, 77], which propagates sparse user edits on a single image to an entire photo collection or video. In our work, we aim to propagate user edits to volumetric data for rendering under different viewpoints. Also relevant is recent work on applying local “rule-based” edits to a trained generative model for images [8]. We are inspired by the above approaches and adapt it to our new 3D neural editing setting.

3. Editing a Conditional Radiance Field

Our goal is to allow user edits of a continuous volumetric representation of a 3D scene. In this section, we first describe a new neural network architecture that more accurately captures the shape and appearance of an object class. We then describe how we update network weights to achieve color and shape editing effects.

To achieve this goal, we build upon the recent neural radiance field (NeRF) representation [45]. While the NeRF representation can render novel views of a particular scene, we seek to enable editing over an entire shape class, e.g., “chairs”. For this, we learn a conditional radiance field model that extends the NeRF representation with latent vectors over shape and appearance. The representation is trained over a set of shapes belonging to a class, and each shape instance is represented by latent shape and appearance vectors. The disentanglement of shape and appearance allows us to modify certain parts of the network during editing.

Let $\mathbf{x} = (x, y, z)$ be a 3D location, $\mathbf{d} = (\phi, \theta)$ be a viewing direction, and $\mathbf{z}^{(s)}$ and $\mathbf{z}^{(c)}$ be the latent shape and color vectors, respectively. Let $(\mathbf{c}, \sigma) = \mathcal{F}(\mathbf{x}, \mathbf{d}, \mathbf{z}^{(s)}, \mathbf{z}^{(c)})$ be the neural network for a conditional radiance field that returns a radiance $\mathbf{c} = (r, g, b)$ and a scalar density σ . The network \mathcal{F} is parametrized as a multi-layer perceptron (MLP) such that the density output σ is independent of the viewing direction, while the radiance \mathbf{c} depends on both position and viewing direction.

To obtain the color at a pixel location for a desired camera location, first, N_c 3D points $\{\mathbf{t}_i\}_{i=1}^{N_c}$ are sampled along a cast ray \mathbf{r} originating from the pixel location (ordered from near to far). Next, the radiance and density values are computed at each sampled point with network \mathcal{F} . Finally, the color is computed by the “over” compositing operation [58]. Let $\alpha_i = 1 - \exp(-\sigma_i \delta_i)$ be the alpha compositing value of sampled point t_i and $\delta_i = t_{i+1} - t_i$ be the distance between the adjacent sampled points. The compositing operation, which outputs pixel color $\hat{\mathbf{C}}$, is the weighted sum:

$$\hat{\mathbf{C}}(\mathbf{r}, \mathbf{z}^{(s)}, \mathbf{z}^{(c)}) = \sum_{i=1}^{N_c-1} c_i \alpha_i \exp\left(-\sum_{j=1}^{i-1} \sigma_j \delta_j\right). \quad (1)$$

Next, we describe details of our network architecture and

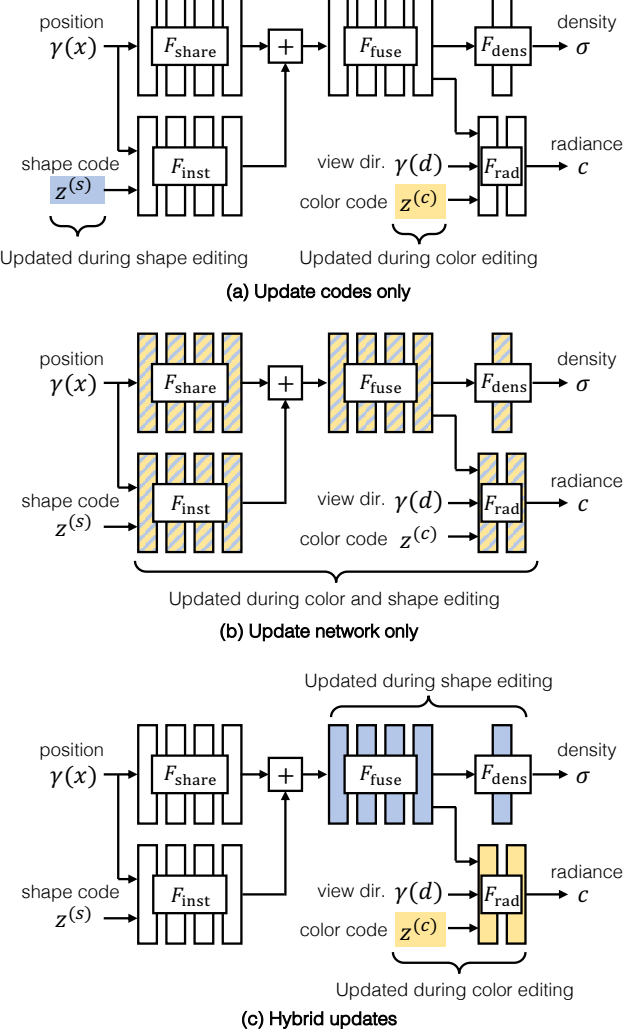


Figure 2: Conditional radiance field network. Our network maps a 3D location \mathbf{x} , viewing direction \mathbf{d} , and instance-specific shape code $\mathbf{z}^{(s)}$ and color code $\mathbf{z}^{(c)}$ to radiance \mathbf{c} and scalar density σ . The network is composed of modular parts for better shape and color disentanglement. We train our network over a collection of 3D objects (Section 3.1). As highlighted, only a subset of the network components need to be updated during editing (Section 3.2).

our training and editing procedures.

3.1. Network with Shared Branch

NeRF [45] finds the inductive biases provided by positional encodings and stage-wise network design critical. Similarly, we find the architectural design choices important and aim for a modular model, providing an inductive bias for shape and color disentanglement. These design choices allow for selected submodules to be finetuned during user editing (discussed further in the next section), enabling more efficient downstream editing. We illustrate our network architecture \mathcal{F} in Figure 2.

First, we learn a category-specific geometric representation with a *shared shape network* $\mathcal{F}_{\text{share}}$ that only operates on the input positional encoding $\gamma(\mathbf{x})$ [45, 70]. To modify the representation for a specific shape, an *instance-specific shape network* $\mathcal{F}_{\text{inst}}$ is conditioned on both the shape code $\mathbf{z}^{(s)}$ and input positional encoding. The representations are added and modified by a *fusion shape network* $\mathcal{F}_{\text{fuse}}$. To obtain the density prediction σ , the output of $\mathcal{F}_{\text{fuse}}$ is passed to a linear layer, the *output density network* $\mathcal{F}_{\text{dens}}$. To obtain the radiance prediction \mathbf{c} , the output of $\mathcal{F}_{\text{fuse}}$ is concatenated with the color code $\mathbf{z}^{(c)}$ and encoded viewing direction $\gamma(\mathbf{d})$ and passed through a two-layer MLP, the *output radiance network* \mathcal{F}_{rad} . We follow Mildenhall *et al.* [45] for training and jointly optimize the latent codes via backpropagation through the network. We provide additional training details in the appendix.

3.2. Editing via Modular Network Updates

We are interested in editing an instance encoded by our conditional radiance field. Given a rendering by the network \mathcal{F} with shape $\mathbf{z}_k^{(s)}$ and color $\mathbf{z}_k^{(c)}$ codes, we desire to modify the instance given a set of user-edited rays. We wish to optimize a loss $\mathcal{L}_{\text{edit}}(\mathcal{F}, \mathbf{z}_k^{(s)}, \mathbf{z}_k^{(c)})$ over the network parameters and learned codes.

Our first goal is to conduct the edit accurately – the edited radiance field should render views of the instance that reflect the user’s desired change. Our second goal is to conduct the edit efficiently. Editing a radiance field is time-consuming, as modifying weights requires dozens of forward and backward calls. Instead, the user should receive interactive feedback on their edits. To achieve these two goals, we consider the following strategies for selecting which parameters to update during editing.

Update the shape and color codes. One approach to this problem is to only update the latent codes of the instance, as illustrated in Figure 2(a). While optimizing such few parameters leads to a relatively efficient edit, as we will show, this method results in a low-quality edit.

Update the entire network. Another approach is to update all weights of the network, shown in Figure 2(b). As we will show, this method is slow and can lead to unwanted changes in unedited regions of the instance.

Hybrid updates. Our proposed solution, shown in Figure 2(c), achieves both accuracy and efficiency by updating specific layers of the network. To reduce computation, we finetune the later layers of the network only. These choices speed up the optimization by only computing gradients over the later layers instead of over the entire network. When editing colors, we update only \mathcal{F}_{rad} and $\mathbf{z}^{(c)}$ in the network, which reduces optimization time by $3.7\times$ over optimizing the whole network (from 972 to 260 seconds). When editing shape, we update only $\mathcal{F}_{\text{fuse}}$ and $\mathcal{F}_{\text{dens}}$, which reduces

optimization time by $3.2\times$ (from 1,081 to 342 seconds).

In Section 4.3, we further quantify the tradeoff between edit accuracy and efficiency. To further reduce computation, we take two additional steps during editing.

Subsampling user constraints. During training, we sample a small subset of user-specified rays. We find that this choice allows optimization to converge faster, as the problem size becomes smaller. For editing color, we randomly sample 64 rays and for editing shape, we randomly sample a subset of 8,192 rays. With this method, we obtain $24\times$ speedups for color edits and $2.9\times$ speedups for shape edits. Furthermore, we find that subsampling user constraints preserves edit quality; please refer to the appendix for additional discussion.

Feature caching. NeRF rendering can be slow, especially when the rendered views are high-resolution. To optimize view rendering during color edits, we cache the outputs of the network that are unchanged during the edit. Because we only optimize \mathcal{F}_{rad} during color edits, the input to \mathcal{F}_{rad} is unchanged during editing. Therefore, we cache the input features for each of the views displayed to the user to avoid unnecessary computation. This optimization reduces the rendering time for a 256×256 image by $7.8\times$ (from 6.2 to under 0.8 seconds).

We also apply feature caching during optimization for shape and color edits. Similarly, we cache the outputs of the network that are unchanged during the optimization process to avoid unnecessary computation. Because the set of training rays is small during optimization, this caching is computationally feasible. We accelerate color edits by $3.2\times$ and shape edits by $1.9\times$.

3.3. Color Editing Loss

In this section, we describe how to perform color edits with our conditional radiance field representation. To edit the color of a shape instance’s part, the user selects a desired color and scribbles a foreground mask over a rendered view indicating where the color should be applied. The user may optionally also scribble a background mask where the color should remain unchanged. These masks do not need to be detailed; instead, a few coarse scribbles for each mask suffice. The user provides these inputs through a user interface, which we discuss in the appendix. Given the desired target color and foreground/background masks, we seek to update the neural network \mathcal{F} and the latent color vector $\mathbf{z}^{(c)}$ for the object instance to respect the user constraints.

Let \mathbf{c}_f be the desired color for a ray \mathbf{r} at a pixel location within the foreground mask provided by the user scribble and let $y_f = \{(\mathbf{r}, \mathbf{c}_f)\}$ be the set of ray color pairs provided by the entire user scribble. Furthermore, for a ray \mathbf{r} at a pixel location in the background mask, let \mathbf{c}_b be the original rendered color at the ray location. Let $y_b = \{(\mathbf{r}, \mathbf{c}_b)\}$ be the set of rays and colors provided by the background user scribble.

Given the user edit inputs (y_f, y_b) , we define our reconstruction loss as the sum of squared-Euclidean distances between the output colors from the compositing operation \hat{C} to the target foreground and background colors:

$$\begin{aligned}\mathcal{L}_{\text{rec}} = & \sum_{(r, c_f) \in y_f} \left\| \hat{C}(r, z^{(s)}, z^{(c)}) - c_f \right\|^2 \\ & + \sum_{(r, c_b) \in y_b} \left\| \hat{C}(r, z^{(s)}, z^{(c)}) - c_b \right\|^2.\end{aligned}\quad (2)$$

Furthermore, we define a regularization term \mathcal{L}_{reg} to discourage large deviations from the original model by penalizing the squared difference between original and updated model weights.

We define our *color editing loss* as the sum of our reconstruction loss and our regularization loss

$$\mathcal{L}_{\text{color}} = \mathcal{L}_{\text{rec}} + \lambda_{\text{reg}} \cdot \mathcal{L}_{\text{reg}}.\quad (3)$$

We optimize this loss over the latent color vector $z^{(c)}$ and \mathcal{F}_{rad} with $\lambda_{\text{reg}} = 10$.

3.4. Shape Editing Loss

For editing shapes, we describe two operations – shape part removal and shape part addition, which we outline next.

Shape part removal. To remove a shape part, the user scribbles over the desired removal region in a rendered view via the user interface. We take the scribbled regions of the view to be the foreground mask, and the non-scribbled regions of the view as the background mask. To construct the editing example, we whiten out the regions corresponding to the foreground mask.

Given the editing example, we optimize a density-based loss that encourages the inferred densities to be sparse. Let σ_r be a vector of inferred density values for sampled points along a ray r at a pixel location and let y_f be the foreground set of rays for the entire user scribble.

We define the density loss $\mathcal{L}_{\text{dens}}$ as the sum of entropies of the predicted density vectors σ_r at foreground ray locations r ,

$$\mathcal{L}_{\text{dens}} = - \sum_{r \in y_f} \sigma_r^\top \log(\sigma_r),\quad (4)$$

where we normalize all density vectors to be unit length. Penalizing the entropy along each ray encourages the inferred densities to be sparse, causing the model to predict zero density on the removed regions.

We define our *shape removal loss* as the sum of our reconstruction, density, and our regularization losses

$$\mathcal{L}_{\text{remove}} = \mathcal{L}_{\text{rec}} + \lambda_{\text{dens}} \cdot \mathcal{L}_{\text{dens}} + \lambda_{\text{reg}} \cdot \mathcal{L}_{\text{reg}}.\quad (5)$$

We optimize this loss over $\mathcal{F}_{\text{dens}}$ and $\mathcal{F}_{\text{fuse}}$ with $\lambda_{\text{dens}} = 0.01$ and $\lambda_{\text{reg}} = 10$.

The above method of obtaining the editing example assumes that the desired object part to remove does not occlude any other object part. We describe an additional slower method for obtaining the editing example which deals with occlusions in the appendix.

Shape part addition. To add a local part to a shape instance, we fit our network to a composite image comprising a region from a new object pasted into the original. To achieve this, the user first selects a original rendered view to edit. Our interface displays different instances under the same viewpoint and the user selects a new instance from which to copy. Then, the user copies a local region in the new instance by scribbling on the selected view. Finally, the user scribbles in the original view to select the desired paste location. For a ray in the paste location in the modified view, we render its color by using the shape code from the new instance and the color code from the original instance. We denote the modified regions of the composite view as the foreground region, and the unmodified regions as the background region.

We define our *shape addition loss* as the sum of our reconstruction and our regularization losses

$$\mathcal{L}_{\text{add}} = \mathcal{L}_{\text{rec}} + \lambda_{\text{reg}} \cdot \mathcal{L}_{\text{reg}}\quad (6)$$

and optimize over $\mathcal{F}_{\text{dens}}$ and $\mathcal{F}_{\text{fuse}}$ with $\lambda_{\text{reg}} = 10$.

We note that this shape addition method can be slow due to the large number of training iterations. In the appendix, we describe a faster but less effective method which encourages inferred densities to match the copied densities.

Please refer to our [video](#) to see our editing demo in action.

4. Experiments

In this section, we show the qualitative and quantitative results of our approach, perform model ablations, and compare our method to several baselines.

Datasets. We demonstrate our method on three publicly available datasets of varying complexity: chairs from the PhotoShape dataset [51] (large appearance variation), chairs from the Aubry chairs dataset [5, 18] (large shape variation), and cars from the GRAF CARLA dataset [63, 17] (single view per instance). For the PhotoShape dataset, we use 100 instances with 40 training views per instance. For the Aubry chairs dataset, we use 500 instances with 36 training views per instance. For the CARLA dataset, we use 1,000 instances and have access to only a single training view per instance. For this dataset, to encourage color consistency across views, we regularize the view direction dependence of radiance, which we further study in the appendix. Furthermore, due to having access to only one view per instance, we forgo quantitative evaluation on the CARLA dataset and instead provide a qualitative evaluation.

Implementation details. Our shared shape network, instance-specific shape network, and fusion shape networks

	PhotoShapes [51]		Aubry <i>et al.</i> [5]	
	PSNR \uparrow	LPIPS \downarrow	PSNR \uparrow	LPIPS \downarrow
1) Single NeRF [45]	17.81	0.435	14.26	0.390
2) + Learned Latent Codes	36.50	0.029	20.93	0.164
3) + Sep. Shape/Color Codes	36.88	0.028	21.54	0.153
4) + Share./Inst. Net (Ours)	37.67	0.022	21.78	0.141
5) NeRF Separate Instances	37.31	0.035	24.15	0.041

Table 1: **Ablation study.** We evaluate our model and several ablations on view reconstruction. Notice how separating the shape and color codes and using the shared/instance network improves the view synthesis quality. Our model even outperforms single-instance NeRF models (each trained on one object).

$\mathcal{F}_{\text{share}}$, $\mathcal{F}_{\text{inst}}$, $\mathcal{F}_{\text{fuse}}$ are all 4 layers deep, 256 channels wide MLPs with ReLU activations and outputs 256 dimensional features. The shape and color codes are both 32-dimensional and jointly optimized with the conditional radiance field model using the Adam optimizer [32] and a learning rate of 10^{-4} . For each edit, we use Adam to optimize the parameters with a learning rate of 10^{-2} . Additional implementation details are included in the appendix.

4.1. Conditional Radiance Field Training

Our method accurately models the shape and appearance differences across instances. To quantify this, we train our conditional radiance field on the PhotoShapes [51] and Aubry chairs [5] datasets and evaluate the rendering accuracy on held-out views over each instance. In Table 1, we measure the rendering quality with two metrics: PSNR and LPIPS [78]. In the appendix, we provide additional evaluation using the SSIM metric [71] in Table 4 and visualize reconstruction results in Figures 16-20. We find our model renders realistic views of each instance and, on the PhotoShapes dataset, matches the performance of training independent NeRF models for each instance.

We report an ablation study over the architectural choices of our method in Table 1. First, we train a standard NeRF [45] over each dataset (Row 1). Then, we add a 64-dimensional learned code for each instance to the standard NeRF and jointly train the code and the NeRF (Row 2). The learned codes are injected wherever positional or directional embeddings are injected in the original NeRF model. While this choice is able to model the shape and appearance differences across the instances, we find that adding separate shape and color codes for each instance (Row 3) and further using a shared shape branch (Row 4) improves performance. Finally, we report performance when training independent NeRF models on each instance separately (Row 5). In these experiments, we increase the width of the layers in the ablations to keep the number of parameters approximately equal across experiments. Notice how our conditional radiance network outperforms all ablations.

Moreover, we find that our method scales well to more training instances. When training with all 626 instances of the PhotoShape dataset, our method achieves reconstruction

	PSNR \uparrow	LPIPS \downarrow
Model Rewriting [8]	18.42	0.325
Finetuning Single-Instance NeRF	29.53	0.068
Only Finetune Color Code	26.29	0.090
Finetuning All Weights	31.00	0.050
Our Method	35.25	0.027

Table 2: **Color editing quantitative results.** We evaluate color editing of a source object instance to match a target instance. Our method outperforms the baselines on all criteria.

PSNR 35.79. We find that the shared shape branch helps our model scale to more instances. In contrast, a model trained without the shared shape branch achieves PSNR 33.91.

4.2. Color Edits

Our method both propagates edits to the desired regions of the instance and generalizes to unseen views of the instance. We show several example color edits in Figure 3. To evaluate our choice of optimization parameters, we conduct an ablation study to quantify our edit quality.

For a source PhotoShapes training instance, we first find an *unseen* target instance in the PhotoShapes chair dataset with an identical shape but a different color. Our goal is to edit the source training instance to match the target instance across all viewpoints. We conduct three edits and show visual results on two: changing the color of a seat from brown to red (Edit 1), and darkening the seat and turning the back green (Edit 2). The details and results of the last edit can be found in the appendix. After each edit, we render 40 views from the ground truth instance and the edited model, and quantify the difference. The averaged results over the three edits are summarized in Table 2.

We find that finetuning only the color code is unable to fit the desired edit. On the other hand, changing the entire network leads to large changes in the shape of the instance, as finetuning the earlier layers of the network can affect the downstream density output.

Next, we compare our method against two baseline methods: editing a single-instance NeRF and editing a GAN.

Single-instance NeRF baseline. We train a NeRF to model the source instance we would like to edit, and then apply our editing method to the single instance NeRF. The single instance NeRF shares the same architecture as our model.

GAN editing baselines. We also compare our method to the 2D GAN-based editing method based on Model Rewriting [8]. We first train a StyleGAN2 model [31] on the images of the PhotoShapes dataset [51]. Then, we project unedited test views of the source instance into latent and noise vectors, using the StyleGAN2 projection method [31]. Next, we invert the source and target view into its latent and noise vectors. With these image/latent pairs, we follow the method of Bau *et al.* [8] and optimize the network to paste the regions of the target view onto the source view. After the optimization

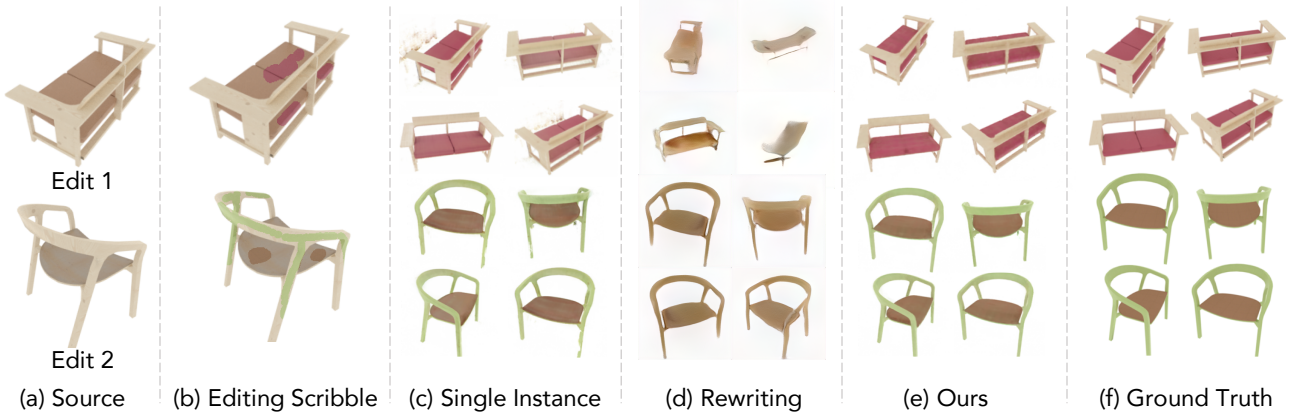


Figure 3: **Color editing qualitative results.** We visualize color editing results where the goal is to match a source instance’s colors to a target. Our method accurately captures the colors of the target instance given scribbles over one view. Notice how (c) Editing a Single-Instance NeRF causes visual artifacts, and (d) Rewriting a GAN [8] fails to propagate the edit to unseen views and generates unrealistic outputs.

	PSNR \uparrow	LPIPS \downarrow	Time (s) \downarrow
Only Finetune Shape Code	22.07	0.119	36.9
Only Finetune $\mathcal{F}_{\text{dens}}$	21.84	0.118	27.2
Finetuning All Weights	20.31	0.117	66.4
Our Method	24.57	0.081	37.4

Table 3: **Shape editing quantitative results.** Notice how our hybrid network update approach achieves high visual edit quality while balancing computational cost.

is complete, we feed the test set latent and noise vectors into the edited model to obtain edited views of our instance. In the appendix, we provide an additional comparison against naive finetuning of the whole generator.

These results are visualized in Figure 3 and in Table 2. A single-instance NeRF is unable to find an change in the model that generalizes to other views, due to the lack of category-specific appearance prior. Finetuning the model can lead to artifacts in other views of the model and can lead to color inconsistencies across views. Furthermore, 2D GAN-based editing methods fail to correctly modify the color of the object or maintain shape consistency across views, due to the lack of 3D representation.

4.3. Shape Edits

Our method is also able to learn to edit the shape of an instance and propagate the edit to unseen views. We show several shape editing examples in Figure 4. Similar to our analysis of color edits, we evaluate our choice of weights to optimize. For a source Aubry chair dataset training instance, we find an unseen target instance with a similar shape. We then conduct an edit to change the shape of the source instance to the target instance, and quantify the difference between the rendered and ground truth views. The averaged results across three edits are summarized in Table 3 and results of one edit are visualized in the top of Figure 4.

We find that the approaches of only optimizing the shape code and only optimizing $\mathcal{F}_{\text{dens}}$ are unable to fit the desired

edit, and instead leave the chair mostly unchanged. Optimizing the whole network leads to removal of the object part, but causes unwanted artifacts in the rest of the object. Instead, our method correctly removes the arms and fills the hole of the chairs, and generalizes this edit to unseen views of each instance.

4.4. Shape/Color Code Swapping

Our model succeeds in disentangling shape and color. When we change the color code input to the conditional radiance field while keeping the shape code unchanged, the resulting rendered views remain consistent in shape. Our model architecture enforces this consistency, as the density output that governs the shape of the instance is independent of the color code.

When changing the shape code input of the conditional radiance field while keeping the color code unchanged, the rendered views remain consistent in color. This is surprising because in our architecture, the radiance of a point is a function of both the shape code and the color code. Instead, the model has learned to disentangle color from shape when predicting radiance. These properties let us freely swap around shape and color codes, allowing for the transfer of shape and appearance across instances; we visualize this in Figure 5.

4.5. Real Image Editing

We demonstrate how to infer and edit extrapolated novel views for a single real image given a trained conditional radiance field. We assume that the single image has attributes similar to the conditional radiance field’s training data (e.g., object class, background). First, we estimate the image’s viewpoint by manually selecting a training set image with similar object pose. In practice, we find that a perfect pose estimation is not required. With the posed input image, we finetune the conditional radiance field by optimizing the stan-

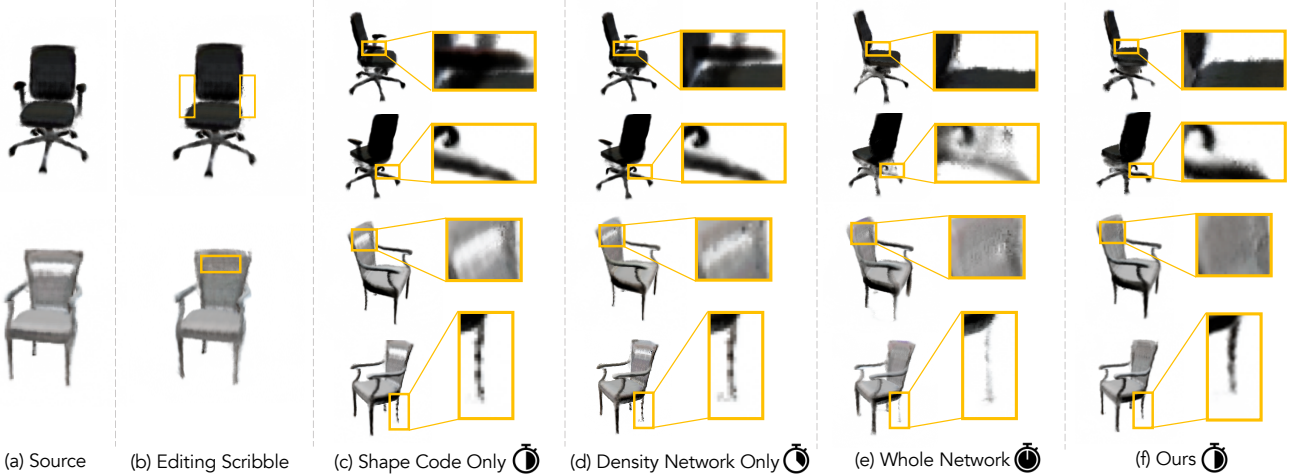


Figure 4: **Shape editing qualitative results.** Our method successfully removes the arms and fills in the hole of a chair. Notice how only optimizing the shape code or branch are unable to fit both edits. Optimizing the whole network is slow and causes unwanted changes in the instance.

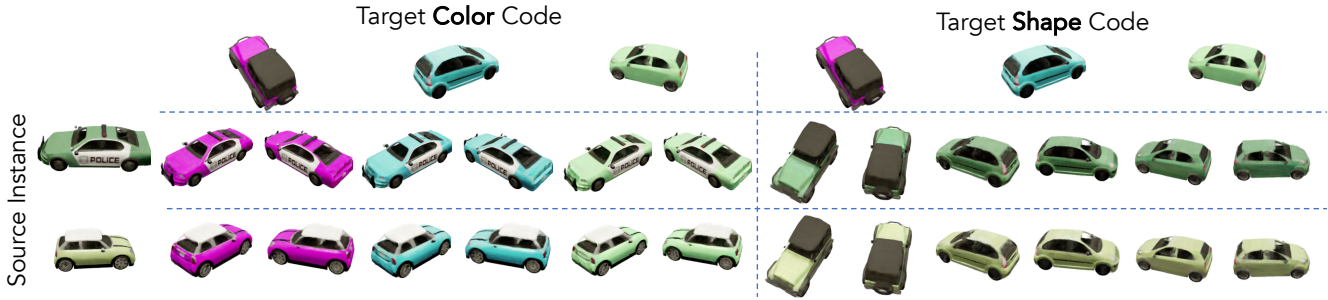


Figure 5: **Shape and color transfer results.** Our model transfers the shape and color from target instances to a given source instance. When a source’s color code is swapped with a target’s, the shape remains unchanged, and vice versa.



Figure 6: **Real image editing results.** Our method first finetunes a conditional radiance field to match a real still image input. Editing the resulting radiance field successfully changes the chair seat color to red and removes two of the chair’s legs.

dard NeRF photometric loss with respect to the image. When conducting this optimization, we first optimize the shape and color codes of the model, while keeping the MLP weights fixed, and then optimize all the parameters jointly. This optimization is more stable than the alternative of optimizing all parameters jointly from the start. Given the finetuned radiance field, we proceed with our editing methods to edit the shape and color of the instance. We demonstrate our results of editing a real photograph in Figure 6.

5. Discussion

We have introduced an approach for learning conditional radiance fields from a collection of 3D objects. Furthermore, we have shown how to perform intuitive editing operations using our learned disentangled representation. One limitation of our method is the interactivity of shape editing. Currently, it takes over a minute for a user to get feedback on their shape edit. The bulk of the editing operation computation is spent on rendering views, rather than editing itself. We are optimistic that NeRF rendering time improvements will help [46, 75]. Another limitation is our method fails to reconstruct novel object instances that are very different from other class instances. Despite these limitations, our approach opens up new avenues for exploring other advanced editing operations, such as relighting and changing an object’s physical properties for animation.

Acknowledgments. Part of this work while SL was an intern at Adobe Research. We would like to thank William T. Freeman for helpful discussions.

References

- [1] Rameen Abdal, Yipeng Qin, and Peter Wonka. Image2stylegan: How to embed images into the stylegan latent space? In *IEEE International Conference on Computer Vision (ICCV)*, 2019. 2
- [2] Aseem Agarwala, Mira Dontcheva, Maneesh Agrawala, Steven Drucker, Alex Colburn, Brian Curless, David Salesin, and Michael Cohen. Interactive digital photomontage. In *ACM SIGGRAPH*, 2004. 2
- [3] Xiaobo An and Fabio Pellacini. Approp: all-pairs appearance-space edit propagation. *ACM Transactions on Graphics (TOG)*, 27(3):40, 2008. 2, 3
- [4] Xiaobo An, Xin Tong, Jonathan D. Denning, and Fabio Pellacini. AppWarp: retargeting measured materials by appearance-space warping. *ACM Trans. Graph.*, 30(6):147, 2011. 2
- [5] Mathieu Aubry, Daniel Maturana, Alexei A Efros, Bryan C Russell, and Josef Sivic. Seeing 3d chairs: exemplar part-based 2d-3d alignment using a large dataset of cad models. In *Proceedings of the IEEE conference on computer vision and pattern recognition*, pages 3762–3769, 2014. 5, 6, 12, 14, 15, 16
- [6] Shai Avidan and Ariel Shamir. Seam carving for content-aware image resizing. In *ACM SIGGRAPH*, 2007. 2
- [7] Connnelly Barnes, Eli Shechtman, Adam Finkelstein, and Dan B Goldman. Patchmatch: A randomized correspondence algorithm for structural image editing. *ACM Transactions on Graphics (TOG)*, 28(3):24, 2009. 2
- [8] David Bau, Steven Liu, Tongzhou Wang, Jun-Yan Zhu, and Antonio Torralba. Rewriting a deep generative model. In *European Conference on Computer Vision (ECCV)*, 2020. 3, 6, 7, 12, 13, 14, 15
- [9] David Bau, Hendrik Strobelt, William Peebles, Jonas Wulff, Bolei Zhou, Jun-Yan Zhu, and Antonio Torralba. Semantic photo manipulation with a generative image prior. *ACM SIGGRAPH*, 38(4), 2019. 2
- [10] Andrew Brock, Theodore Lim, James M Ritchie, and Nick Weston. Neural photo editing with introspective adversarial networks. In *International Conference on Learning Representations (ICLR)*, 2017. 2
- [11] Chris Buehler, Michael Bosse, Leonard McMillan, Steven Gortler, and Michael Cohen. Unstructured lumigraph rendering. In *ACM SIGGRAPH*, page 425–432, New York, NY, USA, 2001. Association for Computing Machinery. 2
- [12] Eric Chan, Marco Monteiro, Petr Kellnhofer, Jiajun Wu, and Gordon Wetzstein. pi-gan: Periodic implicit generative adversarial networks for 3d-aware image synthesis. In *IEEE Conference on Computer Vision and Pattern Recognition (CVPR)*, 2021. 2
- [13] Tao Chen, Zhe Zhu, Ariel Shamir, Shi-Min Hu, and Daniel Cohen-Or. 3-sweep: Extracting editable objects from a single photo. *ACM Trans. Graph.*, 32(6), Nov. 2013. 2
- [14] Zhiqin Chen and Hao Zhang. Learning implicit fields for generative shape modeling. In *IEEE Conference on Computer Vision and Pattern Recognition (CVPR)*, 2019. 2
- [15] Paul E. Debevec, Camillo J. Taylor, and Jitendra Malik. Modeling and rendering architecture from photographs: A hybrid geometry- and image-based approach. In *Proceedings of the 23rd Annual Conference on Computer Graphics and Interactive Techniques, SIGGRAPH ’96*, page 11–20, New York, NY, USA, 1996. Association for Computing Machinery. 2
- [16] Johanna Delanoy, Mathieu Aubry, Phillip Isola, Alexei A. Efros, and Adrien Bousseau. 3d sketching using multi-view deep volumetric prediction. *Proc. ACM Comput. Graph. Interact. Tech.*, 1(1), July 2018. 2
- [17] Alexey Dosovitskiy, German Ros, Felipe Codevilla, Antonio Lopez, and Vladlen Koltun. Carla: An open urban driving simulator. In *Conference on robot learning*, pages 1–16. PMLR, 2017. 5, 12, 13, 15, 17
- [18] Alexey Dosovitskiy, Jost Tobias Springenberg, and Thomas Brox. Learning to generate chairs with convolutional neural networks. In *Proceedings of the IEEE Conference on Computer Vision and Pattern Recognition*, pages 1538–1546, 2015. 5
- [19] Yuki Endo, Satoshi Iizuka, Yoshihiro Kanamori, and Jun Mi-tani. Deepprop: Extracting deep features from a single image for edit propagation. *Computer Graphics Forum*, 35(2):189–201, 2016. 3
- [20] John Flynn, Michael Broxton, Paul Debevec, Matthew Du-Vall, Graham Fyffe, Ryan Styles Overbeck, Noah Snavely, and Richard Tucker. Deepview: High-quality view synthesis by learned gradient descent. In *IEEE Conference on Computer Vision and Pattern Recognition (CVPR)*, 2019. 2
- [21] Kyle Genova, Forrester Cole, Avneesh Sud, Aaron Sarna, and Thomas Funkhouser. Local deep implicit functions for 3d shape. In *IEEE Conference on Computer Vision and Pattern Recognition (CVPR)*, June 2020. 2
- [22] Thibault Groueix, Matthew Fisher, Vladimir G. Kim, Bryan Russell, and Mathieu Aubry. AtlasNet: A Papier-Mâché Approach to Learning 3D Surface Generation. In *Proceedings IEEE Conf. on Computer Vision and Pattern Recognition (CVPR)*, 2018. 2
- [23] Samuel W Hasinoff, Martyna Jóźwiak, Frédéric Durand, and William T Freeman. Search-and-replace editing for personal photo collections. In *IEEE International Conference on Computational Photography (ICCP)*, 2010. 3
- [24] James W Hennessey, Wilmot Li, Bryan Russell, Eli Shechtman, and Niloy J. Mitra. Transferring image-based edits for multi-channel compositing. *ACM Transactions on Graphics*, 36(6), 2017. 2
- [25] Daniel Reiter Horn and Billy Chen. Lightshop: Interactive light field manipulation and rendering. In *Proceedings of the Symposium on Interactive 3D Graphics and Games*, page 121–128, 2007. 2
- [26] Wendy Huther. *3DS Max Chair Modeling – Easy Beginner Tutorial*. https://www.youtube.com/watch?v=w_unzLDGj9U. 1
- [27] Takeo Igarashi, Satoshi Matsuoka, and Hidehiko Tanaka. Teddy: A sketching interface for 3d freeform design. *SIGGRAPH 99 Conference Proceedings*, 109–126. ACM, 99:409–416, 01 1999. 2
- [28] iMeshh. *Blender 2.8 Pro Chair Modeling Guide! - iMeshh Furniture Tutorial*. <https://www.youtube.com/watch?v=Q5XNaxa7jGg>. 1, 12

- [29] Adrian Jarabo, Belen Masia, Adrien Bousseau, Fabio Pellacini, and Diego Gutierrez. How do people edit light fields? *ACM Trans. Graph.*, 33(4), July 2014. [2](#)
- [30] Adrian Jarabo, Belen Masia, and Diego Gutierrez. Efficient propagation of light field edits. In *Ibero-American Symposium in Computer Graphics (SIACG)*, pages 75–80, 2011. [2](#)
- [31] Tero Karras, Samuli Laine, Miika Aittala, Janne Hellsten, Jaakko Lehtinen, and Timo Aila. Analyzing and improving the image quality of StyleGAN. In *IEEE Conference on Computer Vision and Pattern Recognition (CVPR)*, 2020. [6](#), [12](#)
- [32] Diederik P Kingma and Jimmy Ba. Adam: A method for stochastic optimization. *arXiv preprint arXiv:1412.6980*, 2014. [6](#), [12](#)
- [33] Kiriakos N. Kutulakos and Steven M. Seitz. A theory of shape by space carving. *International Journal of Computer Vision (IJCV)*, 38:199–218, 2000. [2](#)
- [34] Anat Levin, Dani Lischinski, and Yair Weiss. Colorization using optimization. In *ACM SIGGRAPH*, pages 689–694, 2004. [2](#)
- [35] Yin Li, Jian Sun, Chi-Keung Tang, and Heung-Yeung Shum. Lazy snapping. *ACM Transactions on Graphics (ToG)*, 23(3):303–308, 2004. [2](#)
- [36] Zhengqi Li, Wenqi Xian, Abe Davis, and Noah Snavely. Crowdsampling the plenoptic function. In *European Conference on Computer Vision (ECCV)*, 2020. [2](#)
- [37] Jerry Liu, Fisher Yu, and Thomas Funkhouser. Interactive 3d modeling with a generative adversarial network. In *2017 International Conference on 3D Vision (3DV)*, pages 126–134. IEEE, 2017. [2](#)
- [38] Shichen Liu, Shunsuke Saito, Weikai Chen, and Hao Li. Learning to infer implicit surfaces without 3d supervision. In H. Wallach, H. Larochelle, A. Beygelzimer, F. d’Alché-Buc, E. Fox, and R. Garnett, editors, *Advances in Neural Information Processing Systems*, 2019. [2](#)
- [39] Shaohui Liu, Yinda Zhang, Songyou Peng, Boxin Shi, Marc Pollefeys, and Zhaopeng Cui. DIST: Rendering deep implicit signed distance function with differentiable sphere tracing. In *IEEE Conference on Computer Vision and Pattern Recognition (CVPR)*, 2020. [2](#)
- [40] Stephen Lombardi, Tomas Simon, Jason Saragih, Gabriel Schwartz, Andreas Lehrmann, and Yaser Sheikh. Neural volumes: Learning dynamic renderable volumes from images. *ACM Trans. Graph.*, 38(4):65:1–65:14, July 2019. [2](#)
- [41] Ricardo Martin-Brualla, Noha Radwan, Mehdi S. M. Sajjadi, Jonathan T. Barron, Alexey Dosovitskiy, and Daniel Duckworth. NeRF in the Wild: Neural Radiance Fields for Unconstrained Photo Collections. In *IEEE Conference on Computer Vision and Pattern Recognition (CVPR)*, 2021. [1](#), [2](#)
- [42] Lars Mescheder, Michael Oechsle, Michael Niemeyer, Sebastian Nowozin, and Andreas Geiger. Occupancy networks: Learning 3d reconstruction in function space. In *IEEE Conference on Computer Vision and Pattern Recognition (CVPR)*, 2019. [2](#)
- [43] Mateusz Michalkiewicz, Jhony K. Pontes, Dominic Jack, Mahsa Baktashmotagh, and Anders Eriksson. Implicit surface representations as layers in neural networks. In *IEEE International Conference on Computer Vision (ICCV)*, 2019. [2](#)
- [44] Ben Mildenhall, Pratul P. Srinivasan, Rodrigo Ortiz-Cayon, Nima Khademi Kalantari, Ravi Ramamoorthi, Ren Ng, and Abhishek Kar. Local light field fusion: Practical view synthesis with prescriptive sampling guidelines. *ACM Transactions on Graphics (TOG)*, 2019. [2](#)
- [45] Ben Mildenhall, Pratul P. Srinivasan, Matthew Tancik, Jonathan T. Barron, Ravi Ramamoorthi, and Ren Ng. NeRF: Representing scenes as neural radiance fields for view synthesis. In *European Conference on Computer Vision (ECCV)*, 2020. [1](#), [2](#), [3](#), [4](#), [6](#), [12](#), [14](#), [17](#), [18](#)
- [46] Thomas Neff, Pascal Stadelbauer, Mathias Parger, Andreas Kurz, Chakravarty R. Alla Chaitanya, Anton Kaplanyan, and Markus Steinberger. DONeRF: Towards real-time rendering of neural radiance fields using depth oracle networks. *arXiv preprint arXiv:2103.03231*, 2021. [8](#)
- [47] Michael Niemeyer, Lars Mescheder, Michael Oechsle, and Andreas Geiger. Differentiable volumetric rendering: Learning implicit 3d representations without 3d supervision. In *Proc. IEEE Conf. on Computer Vision and Pattern Recognition (CVPR)*, 2020. [1](#), [2](#)
- [48] Michael Oechsle, Lars Mescheder, Michael Niemeyer, Thilo Strauss, and Andreas Geiger. Texture fields: Learning texture representations in function space. In *IEEE International Conference on Computer Vision (ICCV)*, 2019. [2](#)
- [49] Kyle Olszewski, Duygu Ceylan, Jun Xing, Jose Echevarria, Zhili Chen, Weikai Chen, and Hao Li. Intuitive, interactive beard and hair synthesis with generative models. In *IEEE Conference on Computer Vision and Pattern Recognition (CVPR)*, 2020. [2](#)
- [50] Jeong Joon Park, Peter Florence, Julian Straub, Richard Newcombe, and Steven Lovegrove. DeepSDF: Learning continuous signed distance functions for shape representation. In *IEEE Conference on Computer Vision and Pattern Recognition (CVPR)*, 2019. [1](#), [2](#)
- [51] Keunhong Park, Konstantinos Rematas, Ali Farhadi, and Steven M. Seitz. Photoshape: Photorealistic materials for large-scale shape collections. *ACM Trans. Graph.*, 37(6), Nov. 2018. [5](#), [6](#), [12](#), [14](#), [17](#)
- [52] Taesung Park, Jun-Yan Zhu, Oliver Wang, Jingwan Lu, Eli Shechtman, Alexei Efros, and Richard Zhang. Swapping autoencoder for deep image manipulation. In *Advances in Neural Information Processing Systems (NeurIPS)*, volume 33, 2020. [2](#)
- [53] Fabio Pellacini, Frank Battaglia, Keith Morley, and Adam Finkelstein. Lighting with paint. *ACM Transactions on Graphics*, 26(2), June 2007. [2](#)
- [54] Songyou Peng, Michael Niemeyer, Lars Mescheder, Marc Pollefeys, and Andreas Geiger. Convolutional occupancy networks. In *European Conference on Computer Vision (ECCV)*, 2020. [2](#)
- [55] Eric Penner and Li Zhang. Soft 3d reconstruction for view synthesis. *ACM Transactions on Graphics (Proc. SIGGRAPH Asia)*, 36(6), 2017. [2](#)
- [56] Patrick Pérez, Michel Gangnet, and Andrew Blake. Poisson image editing. In *ACM SIGGRAPH*, 2003. [2](#)

- [57] Tiziano Portenier, Qiyang Hu, Attila Szabó, Siavash Arjomand Bigdeli, Paolo Favaro, and Matthias Zwicker. Faceshop: Deep sketch-based face image editing. *ACM Transactions on Graphics (TOG)*, 37(4):99:1–99:13, 2018. 2
- [58] Thomas Porter and Tom Duff. Compositing digital images. *ACM SIGGRAPH*, 18(3):253–259, 1984. 1, 3
- [59] Gernot Riegler and Vladlen Koltun. Free view synthesis. In *European Conference on Computer Vision (ECCV)*, 2020. 1, 2
- [60] Carsten Rother, Vladimir Kolmogorov, and Andrew Blake. Grabcut: Interactive foreground extraction using iterated graph cuts. *ACM SIGGRAPH*, 2004. 2
- [61] Shunsuke Saito, Tomas Simon, Jason Saragih, and Hanbyul Joo. PIFuHD: Multi-level pixel-aligned implicit function for high-resolution 3d human digitization. In *IEEE Conference on Computer Vision and Pattern Recognition (CVPR)*, June 2020. 2
- [62] Thorsten-Walther Schmidt, Fabio Pellacini, Derek Nowrouzezahrai, Wojciech Jarosz, and Carsten Dachs-bacher. State of the art in artistic editing of appearance, lighting, and material. In *Eurographics - State of the Art Reports*, 2014. 1, 2
- [63] Katja Schwarz, Yiyi Liao, Michael Niemeyer, and Andreas Geiger. GRAF: Generative radiance fields for 3d-aware image synthesis. In *Advances in Neural Information Processing Systems*, 2020. 1, 2, 5, 12, 15, 17
- [64] Steven M. Seitz and Charles R. Dyer. Photorealistic scene reconstruction by voxel coloring. *International Journal of Computer Vision (IJCV)*, 35:151–173, 1999. 2
- [65] Vincent Sitzmann, Justus Thies, Felix Heide, Matthias Nießner, Gordon Wetzstein, and Michael Zollhöfer. Deepvoxels: Learning persistent 3d feature embeddings. In *IEEE Conference on Computer Vision and Pattern Recognition (CVPR)*, 2019. 2
- [66] Vincent Sitzmann, Michael Zollhöfer, and Gordon Wetzstein. Scene representation networks: Continuous 3d-structure-aware neural scene representations. In *Advances in Neural Information Processing Systems*, 2019. 1, 2
- [67] Pratul P. Srinivasan, Richard Tucker, Jonathan T. Barron, Ravi Ramamoorthi, Ren Ng, and Noah Snavely. Pushing the boundaries of view extrapolation with multiplane images. In *IEEE Conference on Computer Vision and Pattern Recognition (CVPR)*, 2019. 2
- [68] Richard Szeliski and Polina Golland. Stereo matching with transparency and matting. *International Journal of Computer Vision*, 32:45–61, 1999. 2
- [69] Matthew Tancik, Ben Mildenhall, Terrance Wang, Divi Schmidt, Pratul P. Srinivasan, Jonathan T. Barron, and Ren Ng. Learned initializations for optimizing coordinate-based neural representations. In *IEEE Conference on Computer Vision and Pattern Recognition (CVPR)*, 2021. 2
- [70] Ashish Vaswani, Noam Shazeer, Niki Parmar, Jakob Uszkoreit, Llion Jones, Aidan N Gomez, Łukasz Kaiser, and Illia Polosukhin. Attention is all you need. In *Advances in Neural Information Processing Systems*, 2017. 4
- [71] Zhou Wang, Alan C Bovik, Hamid R Sheikh, and Eero P Simoncelli. Image quality assessment: from error visibility to structural similarity. *IEEE Transactions on Image Processing (TIP)*, 13(4):600–612, 2004. 6, 13
- [72] Daniel N. Wood, Daniel I. Azuma, Ken Aldinger, Brian Curless, Tom Duchamp, David H. Salesin, and Werner Stuetzle. Surface light fields for 3d photography. In *ACM SIGGRAPH*, USA, 2000. 2
- [73] Wenqi Xian, Jia-Bin Huang, Johannes Kopf, and Changil Kim. Space-time neural irradiance fields for free-viewpoint video. *arXiv preprint arXiv:2011.12950*, 2020. 2
- [74] Kun Xu, Yong Li, Tao Ju, Shi-Min Hu, and Tian-Qiang Liu. Efficient affinity-based edit propagation using kd tree. *ACM Transactions on Graphics (TOG)*, 28(5):1–6, 2009. 3
- [75] Alex Yu, Rui long Li, Matthew Tancik, Hao Li, Ren Ng, and Angjoo Kanazawa. Plenoctrees for real-time rendering of neural radiance fields. *arXiv preprint arXiv:2103.14024*, 2021. 8
- [76] Alex Yu, Vickie Ye, Matthew Tancik, and Angjoo Kanazawa. pixelNeRF: Neural radiance fields from one or few images. In *IEEE Conference on Computer Vision and Pattern Recognition (CVPR)*, 2021. 2
- [77] Kaan Yücer, Alec Jacobson, Alexander Hornung, and Olga Sorkine. Transfusive image manipulation. *ACM Transactions on Graphics (TOG)*, 31(6):1–9, 2012. 3
- [78] Richard Zhang, Phillip Isola, Alexei A Efros, Eli Shechtman, and Oliver Wang. The unreasonable effectiveness of deep features as a perceptual metric. In *IEEE Conference on Computer Vision and Pattern Recognition (CVPR)*, 2018. 6
- [79] Richard Zhang, Jun-Yan Zhu, Phillip Isola, Xinyang Geng, Angela S Lin, Tianhe Yu, and Alexei A Efros. Real-time user-guided image colorization with learned deep priors. *ACM Transactions on Graphics (TOG)*, 9(4), 2017. 2
- [80] Tinghui Zhou, Richard Tucker, John Flynn, Graham Fyffe, and Noah Snavely. Stereo magnification: Learning view synthesis using multiplane images. In *SIGGRAPH*, 2018. 2
- [81] Jun-Yan Zhu, Philipp Krähenbühl, Eli Shechtman, and Alexei A Efros. Generative visual manipulation on the natural image manifold. In *European Conference on Computer Vision (ECCV)*, 2016. 2
- [82] Jun-Yan Zhu, Zhoutong Zhang, Chengkai Zhang, Jiajun Wu, Antonio Torralba, Joshua B. Tenenbaum, and William T. Freeman. Visual object networks: Image generation with disentangled 3D representations. In *Advances in Neural Information Processing Systems*, 2018. 2

In this appendix, we provide the following:

- Additional experimental details on datasets, model training, and model editing (Section A).
- Additional evaluations of our method and additional ablations. (Section B).
- Additional methods for shape editing. (Section C).
- A description of our user interface. (Section D).
- Additional visualizations of color edits with our approach (Section E).
- Additional visualizations of shape edits with our approach (Section F).
- Additional visualizations of color and shape swapping edits with our approach (Section G).
- A visualization of reconstructions with our conditional radiance field (Section H).
- Changelog (Section I)

A. Additional Experimental Details

Dataset rendering details. For the PhotoShape dataset [51], we use Blender [28] to render 40 views for each instance with a clean background. To obtain the clean background, we obtain the occupancy mask and set everywhere else to white. For the Aubry chairs dataset [5], we resize the images from 600×600 resolution to 400×400 resolution and take a 256×256 center crop. For the CARLA [17] dataset, we train our radiance field on exactly the same dataset as GRAF [63].

Conditional radiance field training details. As in Mildenhall *et al.* [45], we train two networks, a coarse network $\mathcal{F}_{\text{coarse}}$ to estimate the density along the ray, and a fine network $\mathcal{F}_{\text{fine}}$ that renders the rays at test time. We use stratified sampling to sample points for the coarse network and sample a hierarchical volume using the coarse network’s density outputs. The rendered outputs of these networks for an input ray r are given by $\hat{C}_{\text{coarse}}(r)$ and $\hat{C}_{\text{fine}}(r)$, respectively. The networks are jointly trained with the shape and color codes to optimize a photometric loss. During each training iteration, we first sample an object instance $k \in \{1, \dots, K\}$ and obtain the corresponding shape code $\mathbf{z}_k^{(s)}$ and color code $\mathbf{z}_k^{(c)}$. Then, we sample a batch of training rays from the set of all rays R_k belonging to the instance k , and optimize both networks using a photometric loss, which is the sum of squared-Euclidean distances between the predicted colors

and ground truth colors,

$$\begin{aligned} \mathcal{L}_{\text{train}} = \sum_{k=1}^K & \left[\sum_{r \in R_k} \|\hat{C}_{\text{coarse}}(\mathbf{r}, \mathbf{z}_k^{(s)}, \mathbf{z}_k^{(c)}) - C(\mathbf{r})\|_2^2 \right. \\ & \left. + \|\hat{C}_{\text{fine}}(\mathbf{r}, \mathbf{z}_k^{(s)}, \mathbf{z}_k^{(c)}) - C(\mathbf{r})\|_2^2 \right]. \quad (7) \end{aligned}$$

When training all radiance field models, we optimize our parameters using Adam [32] with a learning rate of 10^{-4} , $\beta_1 = 0.9$, $\beta_2 = 0.999$, and $\epsilon = 10^{-8}$. We train our models until convergence, which on average is around 1M iterations.

Conditional radiance field editing details. During editing, we keep the coarse network fixed and edit the fine network $\mathcal{F}_{\text{fine}}$ only. We increase the learning rate to 10^{-2} , and we optimize network components and codes for 100 iterations, keeping all other hyperparameters the same. To obtain training rays, we first randomly select an edited view of the instance, then randomly sample batches of rays from the subsampled set of foreground and background rays.

Conditional radiance field architecture details. Like the original NeRF paper [45], we use skip connections in our architecture: the shape code and embedded input points are fed into the fusion shape network as well as the very beginning of the network.

Furthermore, in our model architecture, we introduce a bottleneck that allows feature caching to be computationally feasible. The input to the color branch is an 8-dimensional vector, which we cache during color editing.

Last, when injecting a shape or color code to a layer, we run the code through a linear layer with ReLU nonlinearity and concatenate the output with the input to the layer.

GAN editing details. In our GAN experiments, we use the default StyleGAN2 [31] configuration on the PhotoShapes dataset and train for 300,000 iterations. For model rewriting [8], we optimize the 8-th layer for 2,000 iterations with a learning rate of 10^{-2} .

View direction dependence. On the CARLA dataset [17, 63], we find that having only one training view per instance can cause color inconsistency across rendered views. To address this, we regularize the view dependence of the radiance c with an additional self-consistency loss that encourages the model to predict for a point x similar radiance across viewing directions d . This loss penalizes, for point x and viewing direction d in the radiance field, the squared difference between the sampled radiance $c(x, d)$ and the average radiance of the point x over all viewing directions. Specifically, given radiance field inputs x, d , we minimize

$$\mathbb{E}_{x \sim p_x, d \sim p_d} \left[\|c(x, d) - \mathbb{E}_{d' \sim p_d} [c(x, d')]\|^2 \right]$$

where p_x is the probability distribution over points x and p_d is the probability distribution over all viewing directions d .

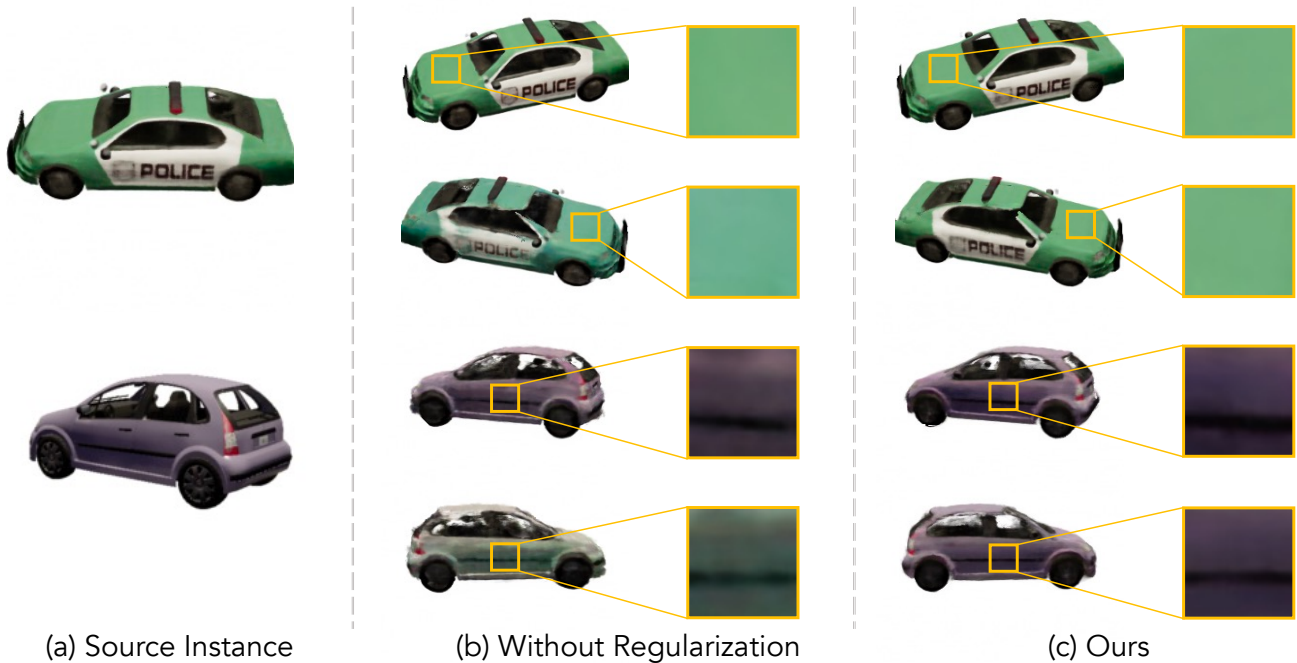


Figure 7: **CARLA [17] dataset radiance view dependence regularization.** We show synthesized views from an unregularized conditional radiance field and a regularized conditional radiance field trained on one view per instance. Notice how the regularized model is consistent in color across views while the unregularized model is not, hallucinating between green and blue (top) and purple and green (bottom).

During training, we approximate this loss by first sampling a training point \mathbf{x} and viewing direction \mathbf{d} , then approximating the inner expectation $\mathbb{E}_{\mathbf{d}' \sim p_{\mathbf{d}}}[\mathbf{c}(\mathbf{x}, \mathbf{d}')]$ by sampling K viewing directions $\mathbf{d}_i \sim p_{\mathbf{d}}$, and taking

$$\mathbb{E}_{\mathbf{d}' \sim p_{\mathbf{d}}}[\mathbf{c}(\mathbf{x}, \mathbf{d}')] \approx \frac{1}{K} \sum_{i=1}^K \mathbf{c}(\mathbf{x}, \mathbf{d}_i).$$

In our experiments, we use $K = 64$. We visualize results with and without this regularization in Figure 7.

B. Additional Evaluations

SSIM metric. We report additional evaluation on model ablation, color editing, and shape editing results using SSIM [71]. Quantitative results can be found in this appendix’s Table 4 (model ablation), Table 5 (color edits), and Table 6 (shape edits).

Subsampling user constraints. During editing, we do not train on the whole foreground and background regions provided by the user, which can potentially decrease the quality of our edits. This is because training on fewer rays can cause the edit to propagate onto unwanted areas. For example, regions which the user specify as background, but are not in the set of sampled rays, can potentially be changed. How-

ever, we find that upon adding this optimization, the average PSNR over the three color edits decreases to 34.49.

Additional GAN editing baselines. We compare our editing method against a naive generator fine-tuning method [8]. The method is identical to the model rewriting method, except instead of conducting a low-rank update of the weights of a particular layer, we freely optimize all the weights of the generator. This optimization is done over 10,000 steps with a learning rate of 10^{-3} . We report our results in Table 5.

C. Additional Shape Editing Methods

Shape removal. For shape removal method described in the main paper, we assume that there is nothing behind an object part that a user scribbles over, allowing us to replace the object part with a white background. However, in practice, a user may wish to remove an object part that is in front of another one. To handle such occlusion, we propose a separate procedure: for each ray in the foreground mask, we zero out the first mode of density along the ray. We define the first mode of density to start at the first point with nonzero-density up to the first subsequent point with zero density. We find that this procedure is effective but can be slow and may leave artifacts of incomplete removal.

Shape addition. For shape addition, our method for recon-

	PhotoShapes [51]			Aubry <i>et al.</i> [5]		
	PSNR \uparrow	SSIM \uparrow	LPIPS \downarrow	PSNR \uparrow	SSIM \uparrow	LPIPS \downarrow
1) Single NeRF [45]	17.81	0.836	0.435	14.26	0.814	0.390
2) + Learned Latent Codes	36.50	0.979	0.029	20.93	0.892	0.164
3) + Sep. Shape/Color Codes	36.88	0.980	0.028	21.54	0.898	0.144
4) + Shar./Inst. Net (Ours)	37.67	0.982	0.022	21.78	0.900	0.141
5) NeRF Separate Instances	37.31	0.972	0.035	24.15	0.963	0.041

Table 4: **Conditional radiance field ablation study.** We evaluate our model and several ablations on novel view synthesis. Notice how separating the shape and color codes and using the shared/instance network improves the view synthesis quality.

	PSNR \uparrow	SSIM \uparrow	LPIPS \downarrow
GAN-Finetuning	19.64	0.704	0.255
Model Rewriting [8]	18.42	0.622	0.325
Finetuning Single-Instance NeRF	29.53	0.955	0.068
Only Finetune Color Code	26.29	0.968	0.090
Finetuning All Weights	31.00	0.957	0.050
Our Method	35.25	0.977	0.027

Table 5: **Color editing quantitative results.** We evaluate color editing of a source object instance to match a target instance. Our method outperforms the baselines on all criteria.

	PSNR \uparrow	SSIM \uparrow	LPIPS \downarrow	Time (s) \downarrow
Only Finetune Shape Code	22.08	0.931	0.119	36.9
Only Finetune $\mathcal{F}_{\text{dens}}$	21.84	0.921	0.118	27.2
Finetuning All Weights	20.31	0.910	0.117	66.4
Our Method	24.57	0.944	0.081	37.4

Table 6: **Shape editing quantitative results.** Notice how our hybrid network update approach achieves high visual edit quality while balancing computational cost.

structuring a composite image leads to effective but slow edits. We propose an additional density-based loss which is faster but less effective in executing the edit. The method for obtaining the editing example is the same, but we now optimize a loss that encourages the density values in the modified regions of the composite view to match with the density values of the regions copied from.

Specifically, let $y_f = \{(r, \sigma_f)\}$ be the set of rays and densities in the foreground mask and $y_b = \{(r, \sigma_b)\}$ be the set of rays and densities in the background mask. Here, σ_f are density values of the rays copied from the new object instance, and σ_b represent density values of the rays from the original instance. Furthermore, let σ_r be the densities predicted by our model for ray r . Again, densities are normalized to sum to one.

We optimize a cross-entropy loss:

$$\mathcal{L}_{\text{dens}} = \sum_{(r, \sigma_f) \in y_f} -\sigma_f^T \log \sigma_r + \sum_{(r, \sigma_b) \in y_b} -\sigma_b^T \log \sigma_r, \quad (8)$$

which encourages the predicted densities to match the target densities for the edited regions and be unchanged for the unedited regions.

D. User Interface

For our user interface, the user first picks an object instance they would like to edit. Our UI then displays several

rendered views of that instance, and the user picks one view to edit. The user can then edit the selected view on an editing panel.

We provide four types of user edits: color edits, shape removal, shape addition, and color/shape transfer. Next, we describe the user interactions for each type of edit.

Color edits. The user chooses the target color from a color palette. Then, the user specifies a foreground mask over the view by clicking the `edit color` button, selecting a brush color, and scribbling over parts of the object. Last, the user specifies the background mask by clicking the `BG` brush and scribbling over where they would like to keep the part unchanged.

Shape removal. The user clicks the `remove shape` button and scribbles over parts of the image they would like to remove.

Shape addition. The user clicks the `add shape` button and several instances to copy shape from will pop up. The user specifies a target instance they would like to copy from, and a view of that instance is shown. Then, the user scribbles over the object part they would like to copy, and clicks on the location of the source instance where they would like to paste.

Shape/Color transfer. The user clicks either the `transfer color` button or the `transfer shape` button and several instances to transfer color/shape from will pop up. Then, the user clicks a desired target instance to transfer color/shape information.

Once the user editing is done, the user will click the `execute` button to execute the desired edit. Our algorithm will then finetune the latent variables and network weights and update the renderings of the edited object. Please see our video [demo](#) for more details.

E. Additional Color Edits

Quantitative color editing evaluation. In this section, we provide the visualizations of all three color edits used for evaluation in the main paper. Visually, we again see that editing a single-instance NeRF leads to visual artifacts and visual inconsistencies across views. Similarly, GAN-based methods are unable to learn an edit that generalizes across



Figure 8: **Color editing qualitative results.** We visualize color editing results where the goal is to match a source instance’s colors to a target. Our method accurately captures the colors of the target instance given scribbles over one view. Notice how (d) Rewriting a GAN [8] fails to propagate the edit to unseen views and results in unrealistic generated outputs. Moreover, editing a single-instance NeRF causes visual floating artifacts (Edit 1) and non-transferring colors (Edit 3).

	Edit 1			Edit 2			Edit 3		
	PSNR	SSIM	LPIPS	PSNR	SSIM	LPIPS	PSNR	SSIM	LPIPS
GAN-Finetuning	21.42	0.744	0.218	20.45	0.730	0.264	18.91	0.686	0.251
Model Rewriting	20.44	0.663	0.301	19.11	0.659	0.322	18.03	0.612	0.315
Finetuning Single-Instance NeRF	28.22	0.933	0.125	28.32	0.956	0.057	29.88	0.964	0.051
Only Finetune Color Code	28.15	0.975	0.054	27.77	0.977	0.097	22.95	0.953	0.120
Finetuning All Weights	33.36	0.970	0.029	32.47	0.967	0.036	27.17	0.936	0.086
Our Method	35.32	0.978	0.024	35.72	0.979	0.027	34.72	0.975	0.031

Table 7: **Color editing quantitative results.** We evaluate color editing of a source object instance to match a target instance. Please refer to Figure 8 (this supplemental) for a visualization of each of the edits. Notice that our method outperforms the baselines for all color edits on all criteria.

views, likely due to their lack of a 3D representation. We visualize the results of the three edits in Figure 8 and quantify them in Table 7.

In Figure 8, the first two rows visualize Edits 1 and 2 discussed in the main paper, and are identical to the visualizations in the main paper’s Figure 3. The last row of Figure 8 visualizes Edit 3, which changes the seat of a chair from brown to green, then the chair back from beige to grey.

In Table 7, we quantify the quality of each of the four edits. The first two main columns correspond to the Edits 1 and 2 discussed in the main paper, while the last two main columns correspond to Edits 3 discussed in Section E.

Single-instance NeRF editing. We also provide an addi-

tional comparison of our method against editing a single-instance NeRF. Here, we change the color of a seat from brown to bright red. Again, we observe that the single-instance NeRF does not learn an edit that generalizes; the model frequently creates red artifacts in chair’s background. In contrast, our model can still learn an edit that successfully propagates to the seat but not to other regions of the scene. We visualize these results in Figure 9.

Additional color editing results. We visualize additional color edits on the Aubry chairs [5] and the CARLA cars [17, 63] datasets in Figure 10.

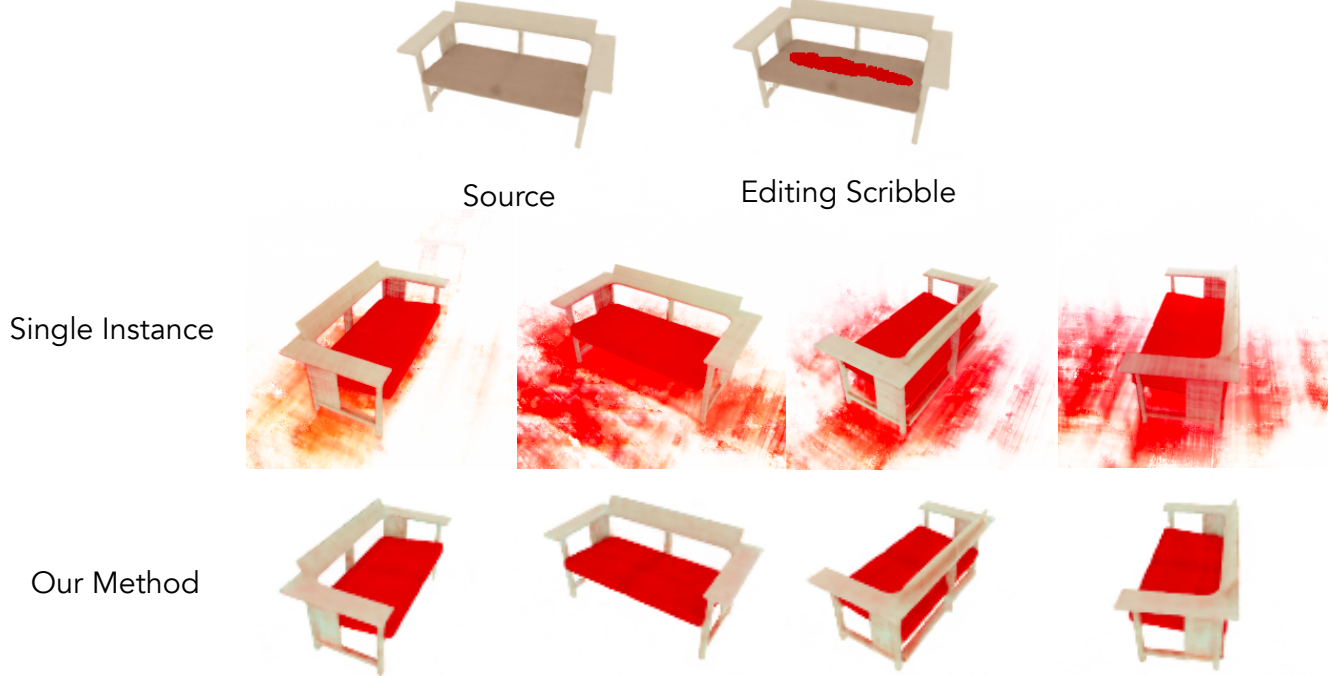


Figure 9: **Single-instance vs. conditional radiance field editing.** We visualize the edit of changing the color of a seat from brown to red. We find that edits on single-instance NeRFs propagate to outside the chair and cause artifacts in the background, whereas our model successfully propagates the edit across only the seat of the chair.

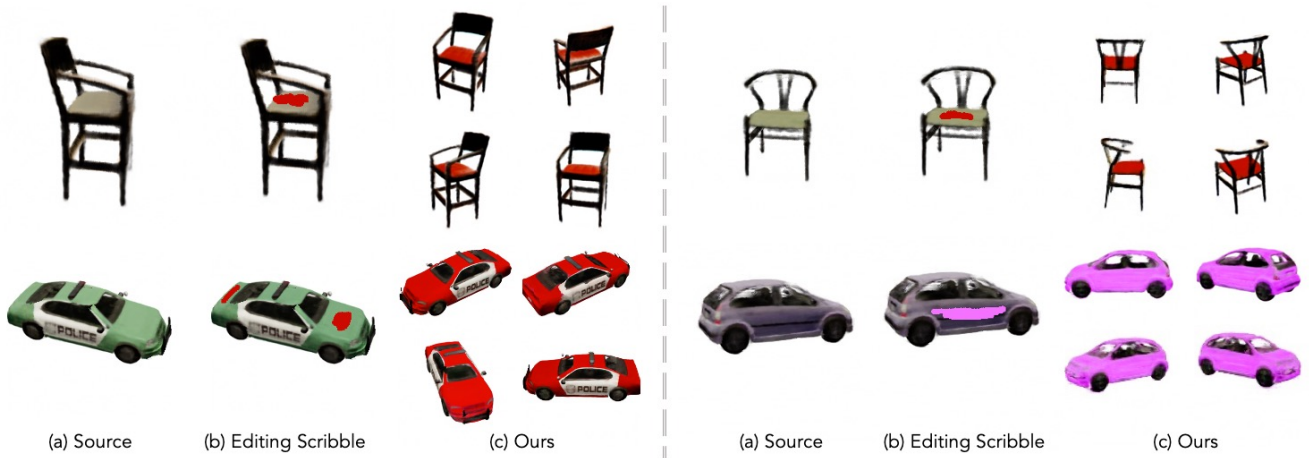


Figure 10: **Additional color editing qualitative results.** Our method successfully colors the seats of two Aubry *et al.* chairs [5] to red, and changes the car body colors to red and pink.

F. Additional Shape Edits

Quantitative color editing evaluation. In this section, we visualize all three shape edits used for evaluation in the main paper. We visualize the results of the three edits in Figure 11 and quantify them in Table 8. Visually, we see that consistent with the main paper, both finetuning the shape code and the shape branch are not enough to change the instance, but finetuning the whole network causes unwanted changes in the instance.

Single-instance NeRF editing. We compare our method against editing a single-instance NeRF [45]. We find that similar to the case with color edits, single-instance NeRFs are unable to learn an edit that generalizes to unseen views, likely due to a lack of a category-level prior. We visualize these results on the PhotoShapes dataset [51] in Figure 12.

Additional shape editing results. We visualize additional shape edits on the PhotoShapes [51] and the CARLA cars datasets [17, 63] in Figure 13.

G. Additional Color/Shape Swapping Edits

We visualize additional shape and color swapping results on the PhotoShapes dataset [51] in Figure 14 (this appendix). Notice again how changing the color code keeps the shape of the instance unchanged, and how changing the shape code keeps the color of the instance unchanged.

H. View Reconstruction

View consistency results. For each of our three datasets, we visualize synthesized views for a fixed instance and observe that the rendered views are all consistent in shape and color. We visualize these results in Figure 15. Notice how in the CARLA dataset [17, 63], despite training on only one image per car instance, the model is able to infer the occluded regions of the car.

Additional reconstruction results. We visualize reconstructed views and depth maps across several instances of the PhotoShapes dataset [51] using our conditional radiance field. For each instance, we render four unseen viewpoints from our model and visually compare them against the ground truth views. We find that our method is able to almost perfectly reconstruct each instance, as well as learn convincing depth estimates of each instance. We visualize reconstructions and depth maps for unseen views in Figures 16-20.

I. Changelog

v1 Initial preprint release.

v2 Update Figure 8 and include additional details in the appendix.



Figure 11: **Shape editing quantitative results.** Notice how only optimizing the shape code or branch are unable to fit both edits. Optimizing the whole network is slow and causes unwanted changes in the instance.

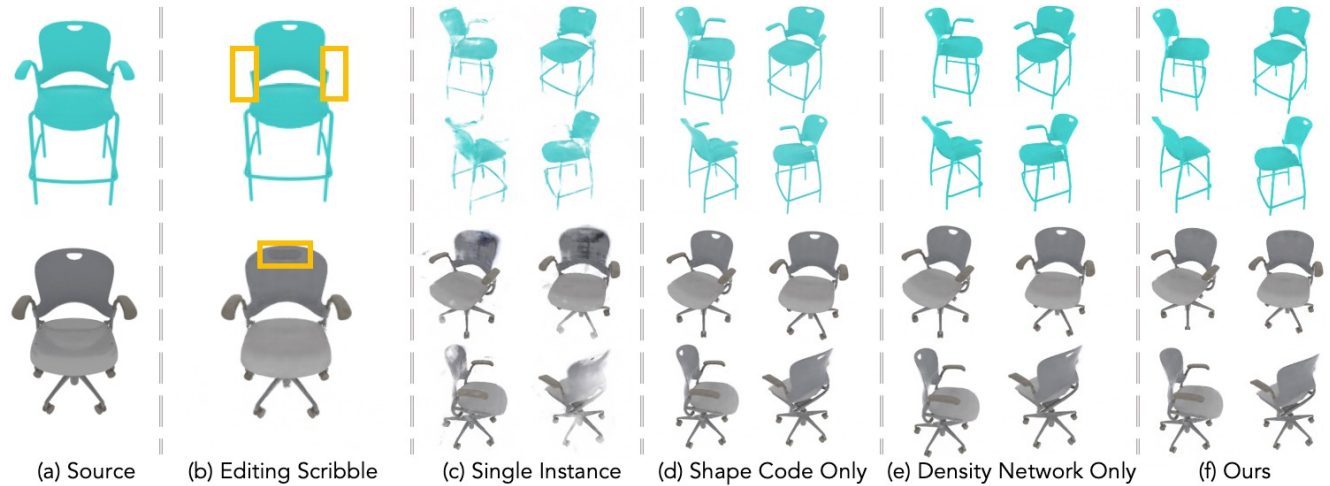


Figure 12: **Shape editing qualitative results.** Our method successfully removes the arms and fills in the hole of a chair. Notice how only optimizing the shape code or branch are unable to fit both edits. Furthermore, editing a single instance NeRF [45] causes unwanted artifacts.

	Edit 1			Edit 2			Edit 3		
	PSNR	SSIM	LPIPS	PSNR	SSIM	LPIPS	PSNR	SSIM	LPIPS
Only Finetune Shape Code	23.52	0.947	0.100	20.18	0.919	0.138	22.52	0.927	0.118
Only Shape Branch	24.59	0.947	0.090	17.96	0.887	0.160	22.94	0.929	0.104
Finetuning All Weights	21.31	0.923	0.100	19.77	0.903	0.128	19.84	0.903	0.123
Our Method	25.68	0.958	0.069	22.97	0.933	0.091	25.04	0.943	0.083

Table 8: **Shape editing quantitative results.** We evaluate shape editing of a source object instance to match a target instance. Please refer to Figure 11 for a visualization of each of the edits. Notice that our method outperforms the baselines for all color edits on all criteria.

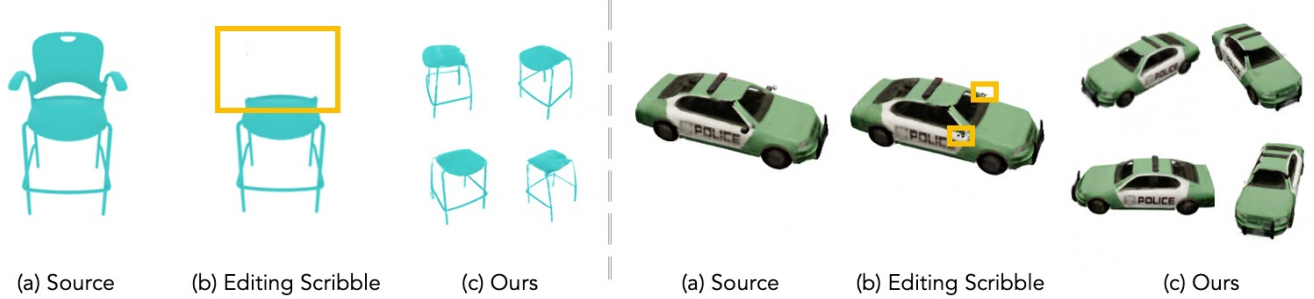


Figure 13: **Shape editing qualitative results.** Our method successfully removes the back and arms of a chair and removes the car mirrors.

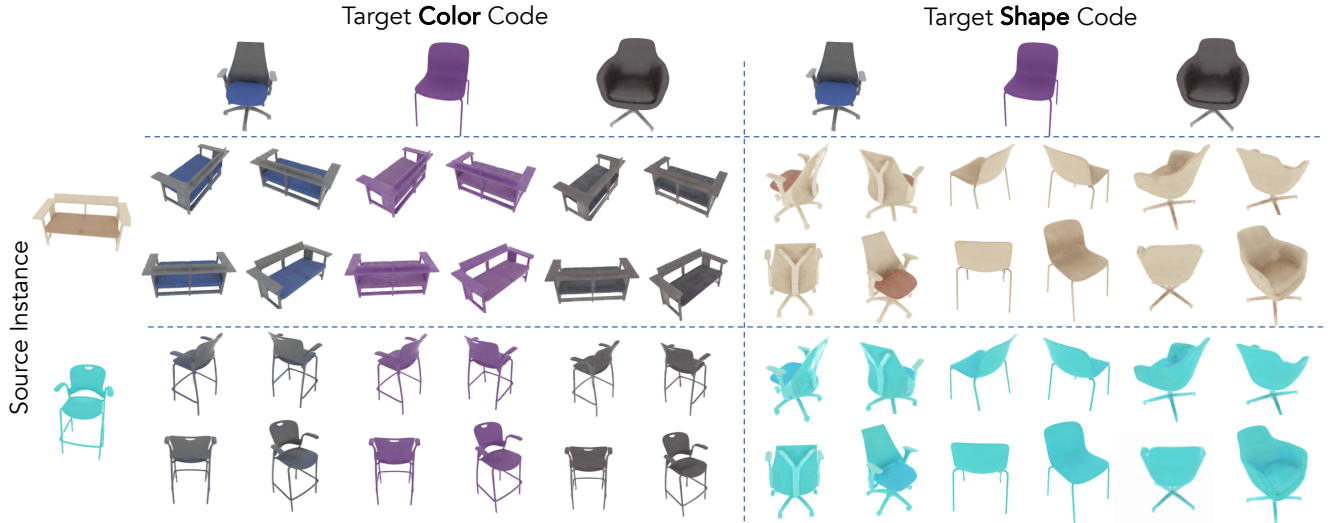


Figure 14: **Shape and color transfer results.** Our model transfers the shape and color from target instances to a given source instance. Notice that when a source's color code is swapped with a target's, the shape remains unchanged, and vice versa.

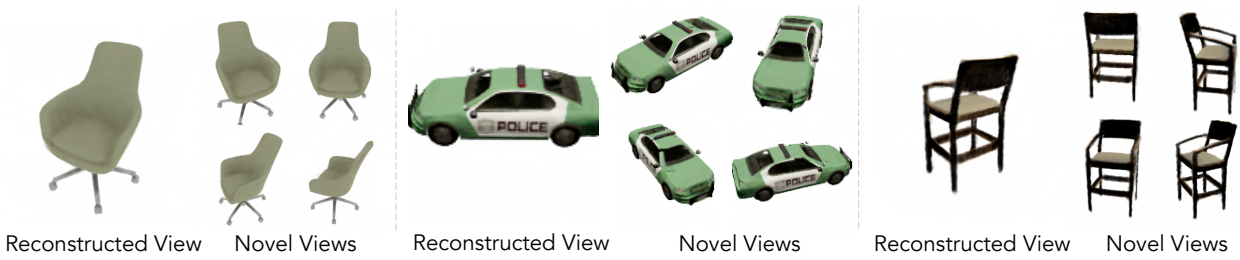


Figure 15: **View reconstruction results.** Our method renders realistic and consistent views across several instances using a single model.

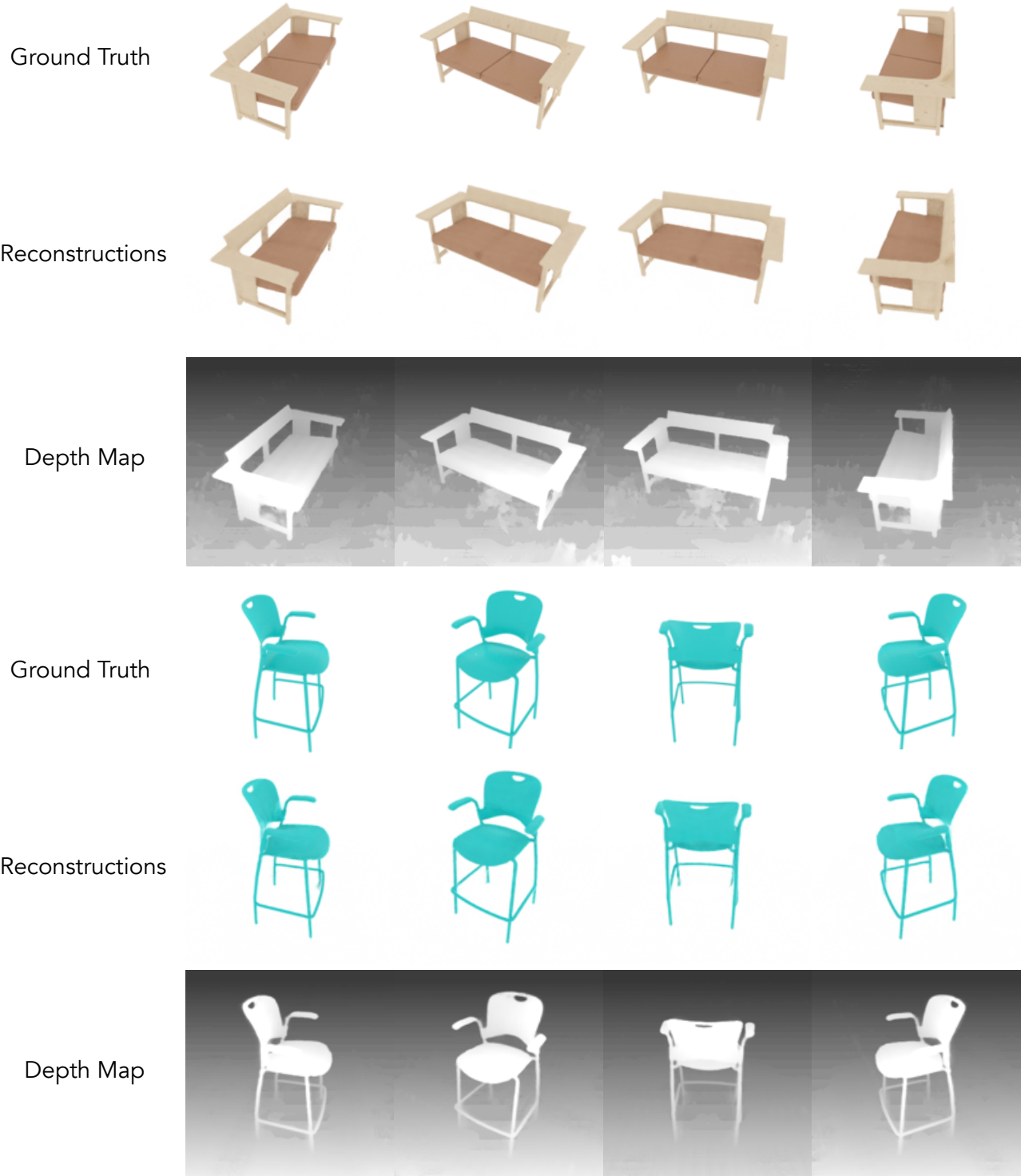


Figure 16: **View reconstruction and depth prediction.** We visualize the rendered views and predicted depth maps of our model on four unseen viewpoints. Notice our model is able to almost perfectly reconstruct the ground truth views.

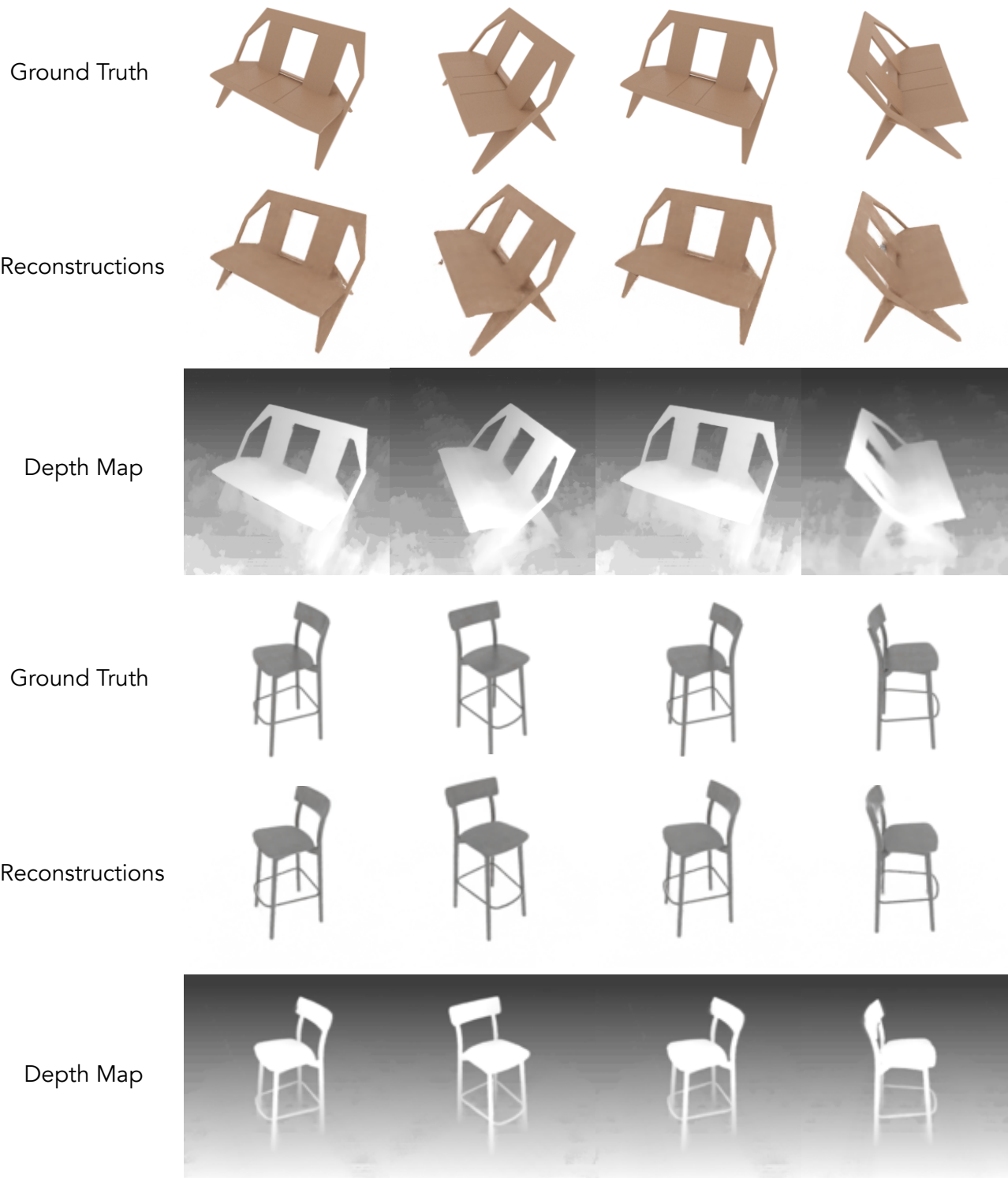


Figure 17: View reconstruction and depth prediction. We visualize the rendered views and predicted depth maps of our model on four unseen viewpoints. Notice our model is able to almost perfectly reconstruct the ground truth views.

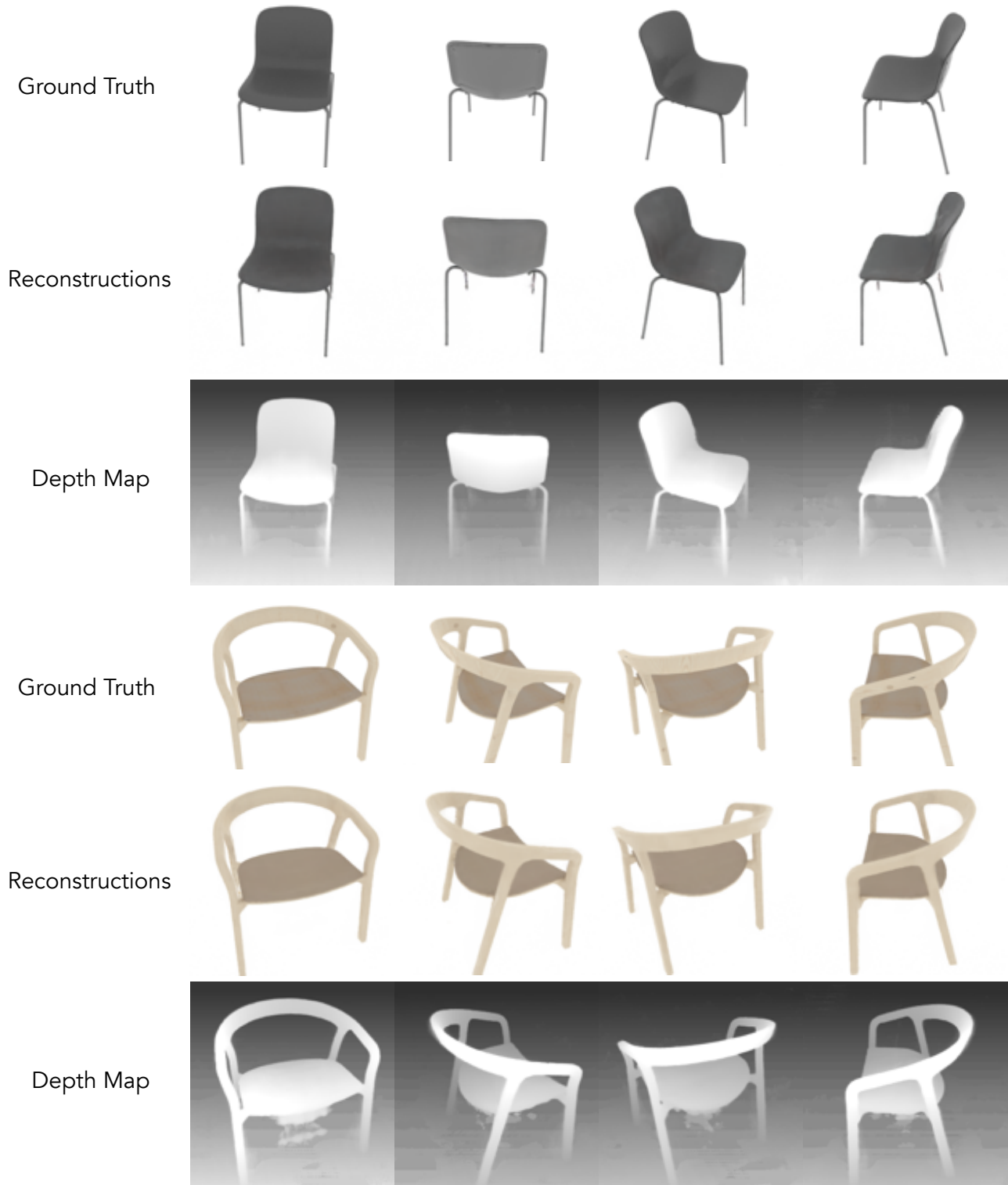


Figure 18: **View reconstruction and depth prediction.** We visualize the rendered views and predicted depth maps of our model on four unseen viewpoints. Notice our model is able to almost perfectly reconstruct the ground truth views.

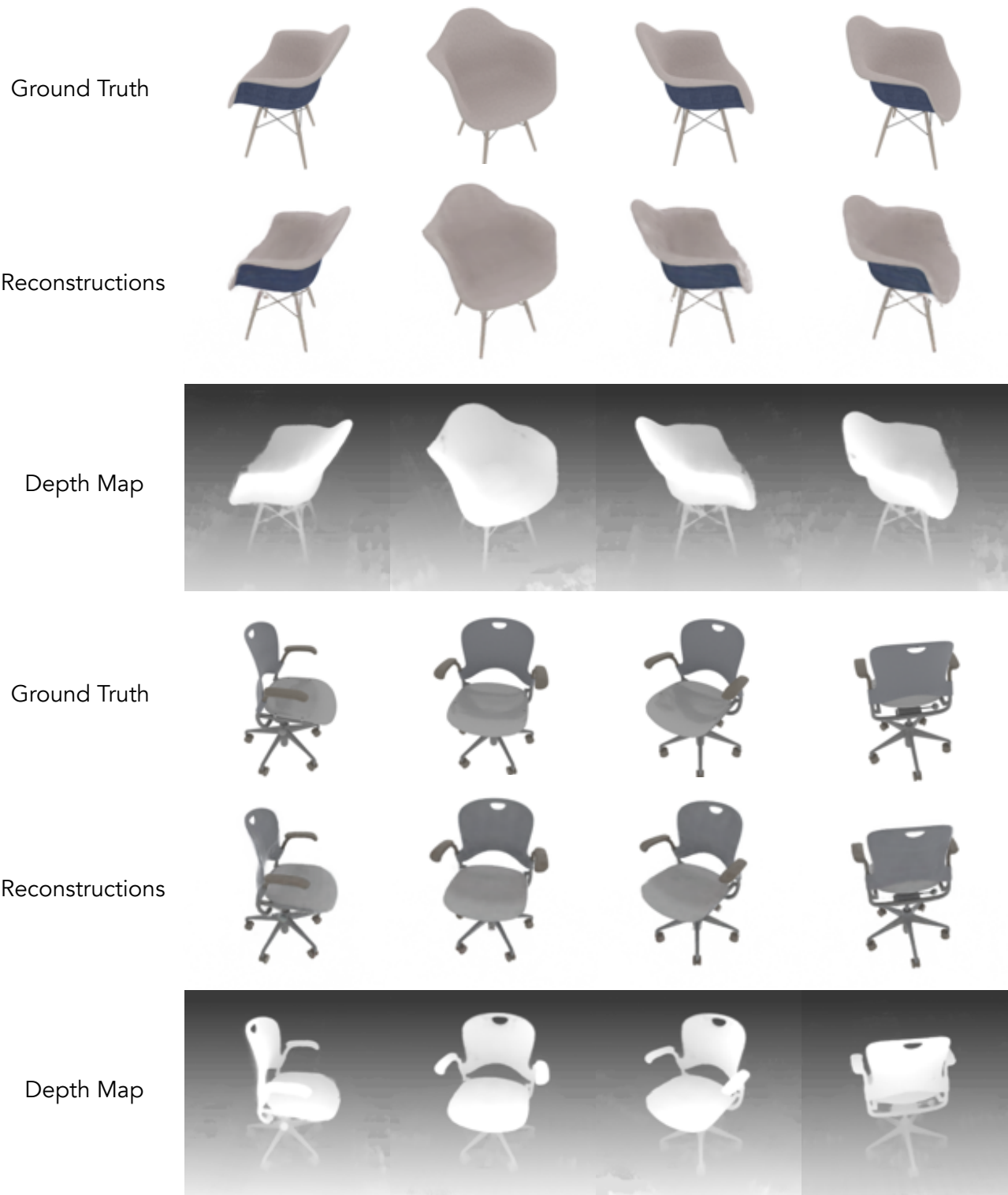


Figure 19: **View reconstruction and depth prediction.** We visualize the rendered views and predicted depth maps of our model on four unseen viewpoints. Notice our model is able to almost perfectly reconstruct the ground truth views.

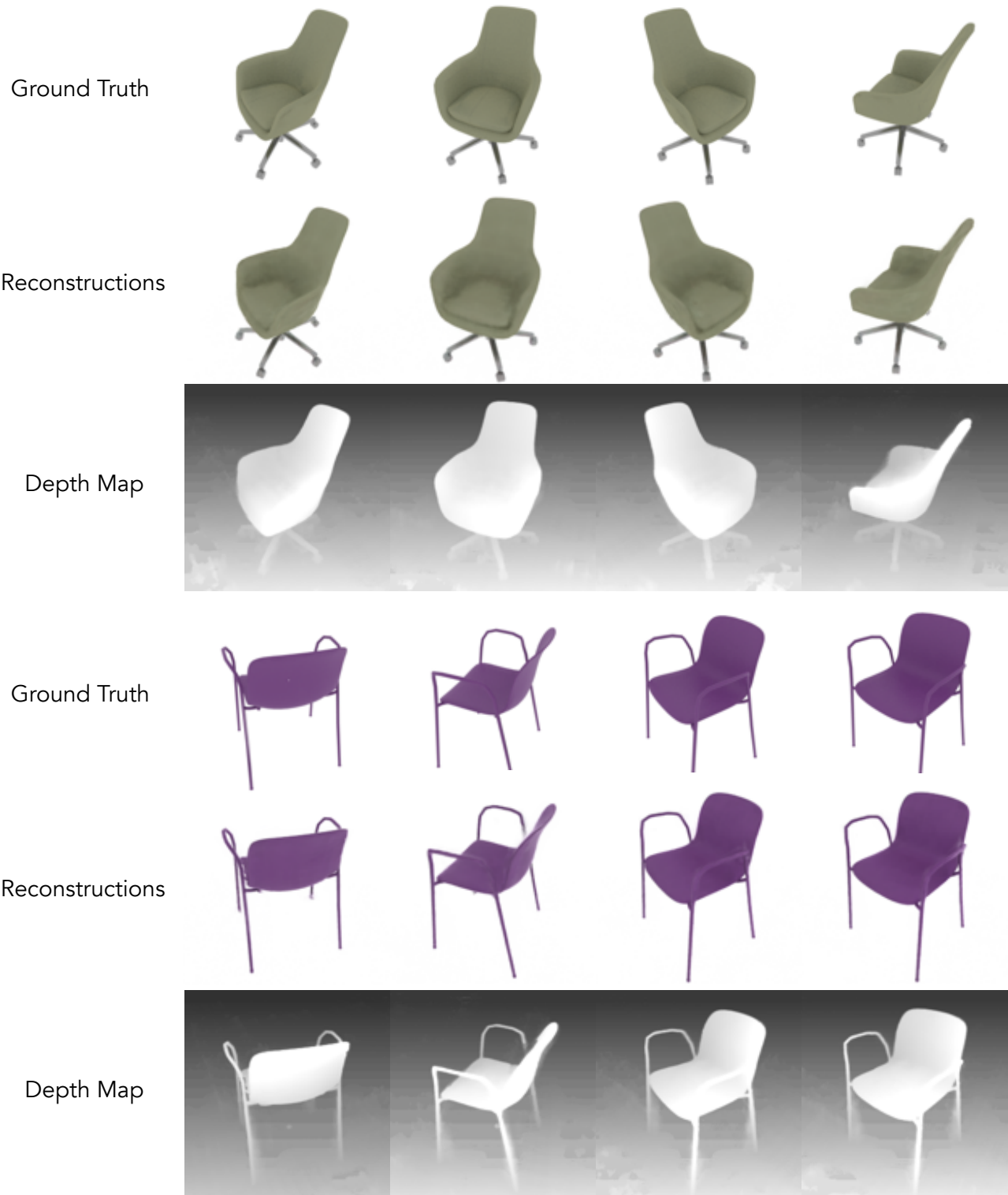


Figure 20: **View reconstruction and depth prediction.** We visualize the rendered views and predicted depth maps of our model on four unseen viewpoints. Notice our model is able to almost perfectly reconstruct the ground truth views.